

Search for new bosons with ytterbium isotope shifts

Menno Door^{1,2*†}, Chih-Han Yeh^{3†}, Matthias Heinz^{4,5,1}, Fiona Kirk^{3,6}, Chunhai Lyu¹, Takayuki Miyagi^{4,5,1}, Julian C. Berengut⁷, Jacek Bieron⁸, Klaus Blaum¹, Laura S. Dreissen^{3,9}, Sergey Eliseev¹, Pavel Filianin¹, Melina Filzinger³, Elina Fuchs^{3,6}, Henning A. Füst^{3,10}, Gediminas Gaigalas¹¹, Zoltán Harman¹, Jost Herkenhoff¹, Nils Huntemann³, Christoph H. Keitel¹, Kathrin Kromer¹, Daniel Lange^{1,2}, Alexander Rischka¹, Christoph Schweiger¹, Achim Schwenk^{4,5,1}, Noritaka Shimizu¹², Tanja E. Mehlstäubler^{3,10,13}

¹Max-Planck-Institut für Kernphysik, Saupfercheckweg 1, Heidelberg, 69117, Germany.

²Heidelberg University, Grabengasse 1, Heidelberg, 69117, Germany.

³Physikalisch-Technische Bundesanstalt, Bundesallee 100, Braunschweig, 38116, Germany.

⁴Department of Physics, Technische Universität Darmstadt, Darmstadt, 64289, Germany.

⁵ExtreMe Matter Institute EMMI, GSI Helmholtzzentrum für Schwerionenforschung GmbH, Darmstadt, 64291, Germany.

⁶Institut für Theoretische Physik, Leibniz Universität Hannover, Appelstraße 2, Hannover, 30167, Germany.

⁷School of Physics, University of New South Wales, Sydney, New South Wales 2052, Australia.

⁸Institute of Theoretical Physics, Jagiellonian University, Kraków, 30-348, Poland.

⁹Department of Physics and Astronomy, LaserLab, Vrije Universiteit Amsterdam, De Boelelaan 1081, Amsterdam, 1081 HV, The Netherlands.

¹⁰Institut für Quantenoptik, Leibniz Universität Hannover, Welfengarten 1, Hannover, 30167, Germany.

¹¹Institute of Theoretical Physics and Astronomy, Vilnius University, Vilnius, 10222, Lithuania.

¹²Center for Computational Sciences, University of Tsukuba, Ibaraki, 305-8577, Japan.

¹³Laboratorium für Nano- und Quantenengineering, Leibniz Universität Hannover, Schneiderberg 39, Hannover, 30167, Germany.

*Corresponding author(s). E-mail(s): menno.door@mpi-hd.mpg.de; chih-han.yeh@ptb.de;

†These authors contributed equally to this work.

Abstract

The Standard Model of particle physics describes the properties of elementary particles and their interactions remarkably well, but in particular does not account for dark matter. Isotope-shift spectroscopy is a sensitive probe of fifth forces and new particles that illuminate the dark matter sector. This method sets bounds on new bosons that couple neutrons and electrons with masses in the keV/c^2 to MeV/c^2 range [1–4]. With increasing spectroscopic precision, such searches are limited by uncertainties of isotope masses and the understanding of nuclear structure. Here, we report on high-precision mass-ratio and isotope-shift measurements of the ytterbium isotopes $^{168,170,172,174,176}\text{Yb}$ that exceed previous measurements [5–8] by up to two orders of magnitude. From these measurements, we extract higher-order changes in the nuclear charge distribution along the Yb isotope chain and use these to benchmark novel *ab initio* calculations. Our measurements set new bounds on the existence of the proposed boson.

Keywords: Isotope-shift spectroscopy, fifth forces, new bosons, high-precision mass spectrometry, *ab initio* atomic and nuclear structure calculations, nuclear charge distributions

Theories beyond the Standard Model (SM) of particle physics are typically probed by high-energy colliders or astrophysical and cosmological observations. Competitive complementary tests can be performed with

high-precision atomic and molecular physics experiments at low energies [4]. In particular, isotope-shift spectroscopy is sensitive to shifts in atomic energy levels induced by hypothetical new bosons that mediate an

additional interaction between neutrons and electrons [1, 3]. Such measurements can be analyzed via the King-plot method, where different atomic transitions are combined in such a way that common nuclear and atomic uncertainties are eliminated. Deviations from the linearity of the King plot indicate effects from new physics or higher-order atomic and nuclear structure. This powerful technique has been successfully used to put bounds on physics beyond the SM. With increasing precision of the frequency measurements, the uncertainties of the nuclear masses [6, 7] become a limiting factor for distinguishing between higher-order SM effects and new physics.

In this work, we present high-precision mass spectrometry and isotope-shift measurements of five stable, spinless ytterbium (Yb) isotopes. Both the mass spectrometry and the isotope-shift spectroscopy are up to two orders of magnitude more precise than previous measurements [5, 7, 8]. The isotope mass ratios, which reach a relative precision of a few 10^{-12} corresponding to a relative precision of 10^{-10} for the isotope shifts, are determined using highly charged Yb ions in the Penning-trap mass spectrometer PENTATRAP [9]. The isotope-shift spectroscopy is performed on Yb⁺ on the $^2S_{1/2} \rightarrow ^2D_{5/2}$ electric quadrupole transition and the highly forbidden $^2S_{1/2} \rightarrow ^2F_{7/2}$ electric octupole transition with a relative precision as low as 10^{-9} . By constructing a generalized King plot [10] including our measurements, we extract a competitive spectroscopic exclusion bound on the coupling strength of potential new bosons to electrons and neutrons.

Combining these precise measurements with atomic structure calculations allows us to investigate higher-order nuclear structure effects in Yb isotopes [11] and to extract changes in the quartic charge radius, $\delta\langle r^4 \rangle$, along the isotopic chain, providing a new window into nuclear deformation. Building on advances in *ab initio* nuclear structure calculations [12–15], we provide a first microscopic description of Yb nuclei starting from chiral effective field theory interactions [16] based on quantum chromodynamics. This method can provide direct insights into the evolution of nuclear charge distributions along isotopic chains towards exotic, neutron-rich nuclei.

Results

Theoretical framework

An isotope shift is the difference in the frequencies of a given atomic transition in two different isotopes of the same element. Here, we consider the $^2S_{1/2} \rightarrow ^2D_{5/2}$ electric quadrupole and the $^2S_{1/2} \rightarrow ^2F_{7/2}$ electric octupole transitions, denoted as α and γ , in singly charged Yb⁺ ions. We consider five stable, even Yb isotopes with mass number $A \in \{168, 170, 172, 174, 176\}$ that contain four neighboring isotope pairs (A, A') with $A' = A + 2$. The corresponding isotope shifts $\nu_\alpha^{A, A'} = \nu_\alpha^A - \nu_\alpha^{A'}$ make up the entries of a four-component vector $\boldsymbol{\nu}_\alpha$ for transition α (and similarly for γ). This vector $\boldsymbol{\nu}_\alpha$ (and $\boldsymbol{\nu}_\gamma$) can

be written as a linear combination of the field shift and mass shift [17], additional higher-order SM-based shifts, and a term induced by the interaction with the potential new boson. Each of these terms can be decomposed into an electronic factor (with subscript α) and a vector encoding the nuclear structure:

$$\boldsymbol{\nu}_\alpha = F_\alpha \boldsymbol{\delta}\langle r^2 \rangle + K_\alpha \boldsymbol{w} + G_\alpha^{(2)} \boldsymbol{\delta}\langle r^2 \rangle^2 + G_\alpha^{(4)} \boldsymbol{\delta}\langle r^4 \rangle + \frac{\alpha_{\text{NP}}}{\alpha_{\text{EM}}} D_\alpha \boldsymbol{h} + \dots \quad (1)$$

The coefficients F , K , $G^{(2)}$, $G^{(4)}$, and D are transition-dependent electronic factors that quantify the multiplicative electronic contribution to the field shift, mass shift, the quadratic field shift, the quartic shift, and a shift induced by a new boson, respectively. The components of \boldsymbol{w} are $w^{A, A'} = m_{172}/m_A - m_{172}/m_{A'} = 1/\eta_A - 1/\eta_{A'}$, denoting the difference between the inverse nuclear masses of the isotopes A and A' with respect to the nuclear mass of ^{172}Yb . $\boldsymbol{\delta}\langle r^n \rangle$ is the four-vector with elements $\delta\langle r^n \rangle^{A, A'} = \langle r^n \rangle^A - \langle r^n \rangle^{A'}$, corresponding to the differences between the n -th moments of the nuclear charge distributions of the isotopes A and A' . $\boldsymbol{\delta}\langle r^2 \rangle^2$ has the components $(\delta\langle r^2 \rangle^2)^{A, A'} = (\delta\langle r^2 \rangle^{A, 176})^2 - (\delta\langle r^2 \rangle^{A', 176})^2$, constructed from squared radius differences of the isotopes A and A' with respect to the reference isotope ^{176}Yb . Additional higher-order SM contributions may also contribute to Eq. (1) at a given experimental accuracy. The quantity $\alpha_{\text{NP}} = (-1)^{s+1} y_n y_e / (4\pi\hbar c)$ is the product of the coupling constants y_n and y_e of the new boson to the neutron and electron, respectively. Together with the mass m_ϕ and spin s of the new boson, they fix the strength of the Yukawa-like potential $V_{\text{ne}}(r) = \hbar c \cdot \alpha_{\text{NP}} \cdot \exp(-r/\lambda_C)/r$ induced by the new boson ϕ in the atom [3]. Here $\lambda_C = \hbar/(m_\phi c)$ is the reduced Compton wavelength of the new boson ϕ . For convenience, we normalize the new coupling α_{NP} by the fine-structure constant $\alpha_{\text{EM}} = e^2/(4\pi\hbar c)$, where e is the elementary charge. $\boldsymbol{h} = -(2, 2, 2, 2)$ is the vector of neutron number differences within the neighboring isotope pairs.

Usually, only the first two terms in Eq. (1) contribute significantly. With the isotope-shift measurements for two transitions α and γ , one can eliminate $\boldsymbol{\delta}\langle r^2 \rangle$ from Eq. (1) so that the first two terms yield the linear King relation [3, 17]

$$\tilde{\boldsymbol{\nu}}_\gamma \approx F_{\gamma\alpha} \tilde{\boldsymbol{\nu}}_\alpha + K_{\gamma\alpha} \mathbf{1}. \quad (2)$$

Here we defined the mass-normalized $\tilde{\boldsymbol{\nu}}_\gamma = \boldsymbol{\nu}_\gamma/\boldsymbol{w}$ (and likewise for other transitions), $\mathbf{1} = (1, 1, 1, 1)$, and $F_{\gamma\alpha} = F_\gamma/F_\alpha$, which also enters $K_{\gamma\alpha} = K_\gamma - F_{\gamma\alpha} K_\alpha$. Deviations from Eq. (2) indicate the presence of additional terms beyond the leading-order field shift and mass shift, as indicated in Eq. (1).

Experimental results

The nuclear mass ratios η_A of ytterbium isotopes are determined from the cyclotron frequency ratios of highly charged Yb^{42+} ions measured at the cryogenic Penning-trap mass spectrometer PENTATRAP [9, 18, 19], and their calculated electron binding energies. A simplified schematic of the measurement setup is shown in Fig. 1 d. The determination of the cyclotron frequency ν_c of the two isotope ions allows one to extract their ionic mass ratio via $R_A^{\text{CF}} = \nu_c(^{172}\text{Yb}^{42+})/\nu_c(^A\text{Yb}^{42+}) = m(^A\text{Yb}^{42+})/m(^{172}\text{Yb}^{42+})$. The determination of the free cyclotron frequency relies on the measurement of all three eigenfrequencies of the trapped ion via $\nu_c^2 = \nu_+^2 + \nu_z^2 + \nu_-^2$ [20], namely, the trap-modified cyclotron frequency, the axial frequency, and the magnetron frequency. A resonance circuit attached to a trap electrode is used to amplify the image current induced by the axial motion (parallel to the trap axis) of a trapped ion to determine its frequency. The radial frequencies ν_+^2 and ν_-^2 are measured indirectly by coupling these eigenmodes to the axial eigenmode. Ions are transported between positions by trapping potential variation and are stored in the same potential setting within one trap to minimize systematic differences between measurements comparing two isotopes. In order to account for the difference in the respective axial frequencies due to equal trapping potentials but different charge-to-mass ratios of the ions, the resonance frequency of the detection system is tuned instead [21].

The use of highly charged ions significantly reduces the relative statistical uncertainty of R_A^{CF} to 2–4 parts per trillion. By accounting for the calculated electron binding energies $E_{172}^{(28)} = 350\,773(5)$ eV and $E_{172}^{(70)} = 382\,301(16)$ eV [22] of the 28 electrons in the $^{172}\text{Yb}^{42+}$ ion and 70 electrons in the ^{172}Yb atom, respectively, as well as the neutral mass of $m(^{172}\text{Yb})$ [23] and the electron mass m_e [24], one can derive the necessary nuclear mass ratios η_A to similar accuracies via Eq. (4) shown in the Methods. Their final values are given in Tab. 1 with relative uncertainties of of 4×10^{-12} , corresponding to an uncertainty of 0.3 Hz on the isotope shifts. For comparison, previous mass determinations affected the King plot analysis at a level of 3–30 Hz.

To make use of the new mass uncertainties we improve the uncertainties of the isotope shifts by performing absolute frequency measurements of the α and γ transitions for the five isotopes. Singly charged ytterbium ions are trapped in a segmented, linear radio-frequency Paul trap [25, 26]. The excitation lasers near wavelengths of 411 nm and 467 nm are locked to ultra-low-expansion (ULE) cavities and to a cryogenic silicon cavity (Si-cavity) [27] via a frequency comb. The transition frequencies in even isotopes of ytterbium are linearly dependent on the magnitude of the applied magnetic field. We apply a bias field of 65 μT and measure two Zeeman components with opposite magnetic field sensitivity to obtain the transition frequency at zero magnetic field. Since

the $^2F_{7/2}$ state in the even isotopes of Yb^+ has a long radiative lifetime of 1.6 years [28], high-intensity laser light is needed to drive the γ transition, inducing large ac-Stark shifts. To obtain the unperturbed transition frequency, we measure at two different light intensities and extrapolate to zero laser intensity.

The absolute transition frequencies are obtained with optical frequency ratio measurements by referencing to the γ transition between the $F = 0$ and $F = 3$ hyperfine states of the $^{171}\text{Yb}^+$ isotope [29]. From the measurements, we obtain isotope shifts with uncertainties below 6 Hz and 16 Hz for the α and the γ transitions, respectively, see Tab. 1. A simplified scheme of the experimental setup is depicted in Fig. 1 a.

For details on the mass-ratio measurements, spectroscopic measurements, systematic shifts, and uncertainties, see the Methods and the Supplementary Material.

King plot analysis

Given the two orders of magnitude improvement in the precision of our nuclear mass measurements, it has become beneficial to construct an ytterbium King plot from the mass-normalized isotope shifts (see below Eq. (2)). In Fig. 1 b,c we show the King plot using our isotope-shift measurements of the γ transition (denoted $\tilde{\nu}_{\gamma\text{PTB}}$) and the α transition (denoted $\tilde{\nu}_{\alpha\text{PTB}}$). From the King-plot analysis, we observe deviations from linearity averaging to 20.17(2) kHz.

To determine the origin of the nonlinearity in the King plot, we perform a nonlinearity decomposition analysis together with the isotope shift measurements from Ref. [8], α_{MIT} and γ_{MIT} , plus additional transitions for which kHz- or sub-kHz-precision isotope shift data is available. These are the $^2S_{1/2} \rightarrow ^2D_{3/2}$ transition in Yb^+ [6] (denoted β), $^1S_0 \rightarrow ^3P_0$ in Yb [30] (denoted δ), and $^1S_0 \rightarrow ^1D_2$ in Yb [31] (denoted ϵ). In total, we construct 7 mass-normalized isotope shift vectors $\tilde{\nu}_\tau$, with $\tau \in \{\alpha_{\text{PTB}}, \alpha_{\text{MIT}}, \beta, \gamma_{\text{PTB}}, \gamma_{\text{MIT}}, \delta, \epsilon\}$. Since these vectors are four-vectors, four being the number of isotope pairs, each of them is uniquely described by its projection onto four basis vectors. For simplicity, we choose the basis vectors $\tilde{\nu}_\delta$ and $\mathbf{1}$, which span the plane of King linearity (see Eq. (2), with $\alpha \rightarrow \delta$), and $\mathbf{\Lambda}_+ \propto (\tilde{\nu}_\delta^c - \tilde{\nu}_\delta^b, \tilde{\nu}_\delta^a - \tilde{\nu}_\delta^d, \tilde{\nu}_\delta^d - \tilde{\nu}_\delta^a, \tilde{\nu}_\delta^b - \tilde{\nu}_\delta^c)$ and $\mathbf{\Lambda}_- \propto (\tilde{\nu}_\delta^d - \tilde{\nu}_\delta^b, \tilde{\nu}_\delta^a - \tilde{\nu}_\delta^c, \tilde{\nu}_\delta^b - \tilde{\nu}_\delta^d, \tilde{\nu}_\delta^c - \tilde{\nu}_\delta^a)$, normalized to 1 Hz, which are orthogonal to this plane. Here we used the notation $a = (168, 170)$, $b = (170, 172)$, $c = (172, 174)$, $d = (174, 176)$ for brevity. We obtain

$$\tilde{\nu}_\tau = (\tilde{\nu}_\delta \ \mathbf{1} \ \mathbf{\Lambda}_+ \ \mathbf{\Lambda}_-) \begin{pmatrix} F_{\tau\delta} & K_{\tau\delta} & \lambda_+^{(\tau)} & \lambda_-^{(\tau)} \end{pmatrix}^T, \quad (3)$$

with $F_{\tau\delta}$ and $K_{\tau\delta}$ as given in Eq. (2), and a set of coordinates $(\lambda_+^{(\tau)}, \lambda_-^{(\tau)})$ characterizing the deviation of the isotope shift ν_τ from the linear relation in Eq. (2). As shown in Fig. 2 a, the data points $(\lambda_+^{(\tau)}, \lambda_-^{(\tau)})$ lie, to a good approximation, on a line through the origin of the

Table 1: Measured values of the mass ratios and isotope shifts. Columns 2 and 3 show the cyclotron frequency ratios and nuclear mass ratios of the even, stable ytterbium isotopes relative to the nuclear mass of isotope $A = 172$, respectively. The mass ratios are determined from measured cyclotron frequency ratios of trapped ytterbium ions with charge state $42+$, which are then corrected according to Eq. (4) to nuclear mass ratios. Columns 4 and 5 show the isotope shifts $\nu^{A,A+2} = \nu^A - \nu^{A+2}$ of the $^2S_{1/2} \rightarrow ^2D_{5/2}$ electric quadrupole (α) transition and the $^2S_{1/2} \rightarrow ^2F_{7/2}$ electric octupole (γ) transition, respectively, in units of Hz.

Isotope A	$R_A^{\text{CF}} = \nu_{c,172}/\nu_{c,A}$	$\eta_A = m_A/m_{172}$	$\nu_{\alpha\text{PTB}}^{A,A+2}$ [Hz]	$\nu_{\gamma\text{PTB}}^{A,A+2}$ [Hz]
168	0.976 717 951 145 (4)	0.976 715 921 748 (4)	2179098868.0 (5.3)	-4438159671.1 (15.7)
170	0.988 356 814 144 (4)	0.988 355 799 257 (4)	2044851281.0 (4.9)	-4149190501.1 (15.7)
172	–	–	1583064149.3 (4.8)	-3132320458.1 (15.7)
174	1.011 648 196 817 (4)	1.011 649 212 140 (4)	1509053195.8 (4.7)	-2976392045.3 (15.7)
176	1.023 303 526 697 (4)	1.023 305 557 965 (4)	–	–

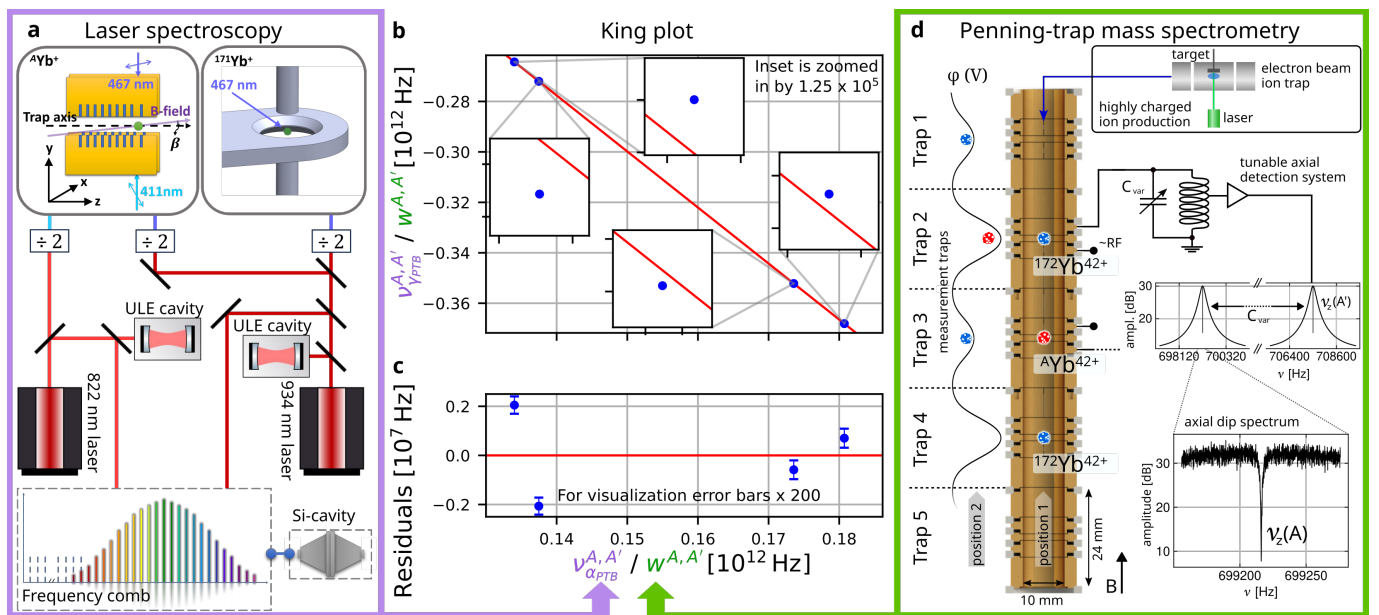


Fig. 1: Scheme of experimental setups and the King-plot analysis. **a** Laser spectroscopy setup for the optical frequency ratio measurements of the transitions near 411 nm (α) and 467 nm (γ). The laser fields with wavelengths near 822 nm and 934 nm are first stabilized to an ultra-low expansion (ULE) cavity for short-term frequency stability and then locked to a cryogenic silicon cavity (Si-cavity). The second harmonic conversions of the lasers are focused to interrogate the ion (denoted as green balls in the simplified trap schematics). **b** King plot of the isotope shifts of the $^2S_{1/2} \rightarrow ^2F_{7/2}$ electric octupole (γ) transition with respect to the isotope shifts of the $^2S_{1/2} \rightarrow ^2D_{5/2}$ electric quadrupole (α) transition normalized with the inverse mass-ratio difference $w^{A,A'}$. The insets are magnified by a factor of 1.25×10^5 . **c** Residuals of the linear fit in the King plot. For visibility of the values in the y-axis, the uncertainties for both axes are multiplied by a factor of 200. From the linear fit, we find deviations from linearity averaging to 20.17(2) kHz. **d** Penning-trap setup for the determination of cyclotron frequency ratios. Three highly charged ions (blue and red), produced by an electron beam ion trap, are extracted and stored in an $A'-A-A'$ sequence to determine cyclotron frequency ratios in parallel in two Penning traps. The tunable image-current detection system allows for the determination of the trap eigenfrequencies of different isotopes at equal charge state and equal trapping potential.

(λ_+ , λ_-) plane (see solid black line with the label “Linear fit to residuals”). This implies that the tension of the Yb isotope-shift data with respect to King linearity (see Eq. (2)) can to a large extent be explained by a non-linearity source (new physics, the quadratic field shift, or the quartic shift, for example) with the appropriate slope λ_-/λ_+ in the decomposition plot. Comparing the slope of the linear fit to the slopes predicted by the new

physics term (dash-dotted line, uncertainties are smaller than the width of the line) and the quadratic field shift $\delta\langle r^2 \rangle^2$ (dotted line, derived from experimental data for $\delta\langle r^2 \rangle$ [32], again, uncertainties are smaller than the width of the line), we conclude that neither can be the leading source of the nonlinearity in the Yb King plot (for details, see the Supplementary Material). As suggested in Ref. [11], another candidate is nuclear deformation,

in particular $\delta\langle r^4 \rangle$, which we predict using an *ab initio* approach.

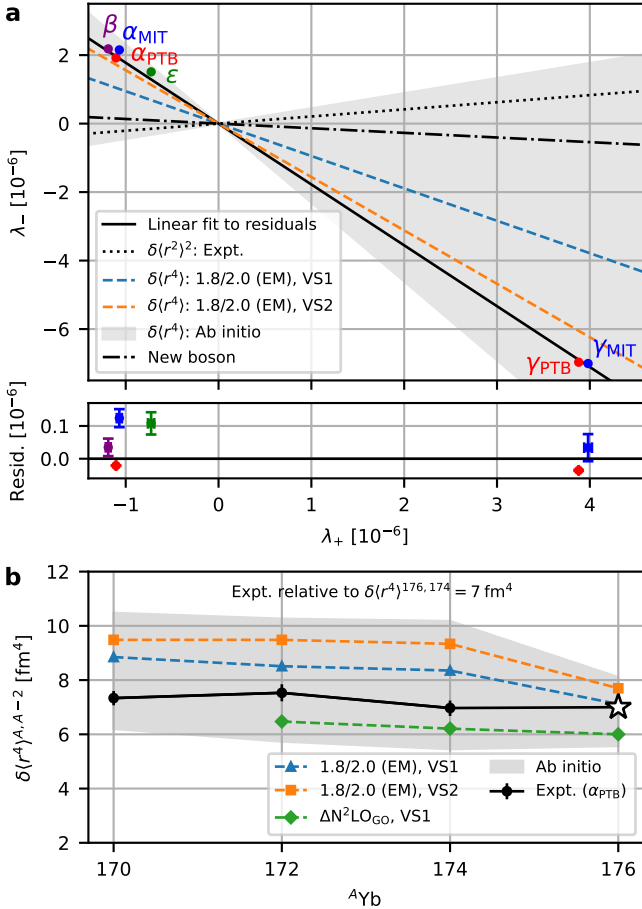


Fig. 2: Nonlinearity decomposition plot and the extracted trend of nuclear deformation, $\delta\langle r^4 \rangle$. **a** Observed and predicted nonlinearities in the (λ_+, λ_-) plane. The isotope-shift data of the transitions α_{PTB} , β , γ_{PTB} , γ_{MIT} , and ϵ , normalized to the δ transition, are included in the single-source linear fit (solid line) whose slope is compared to the predicted slopes for the $\delta\langle r^2 \rangle^2$ (dotted), $\delta\langle r^4 \rangle$ (dashed lines and gray band based on predictions in **b**), as well as new physics (dash-dotted) nonlinearities. The residuals of the single-source linear fit are shown in the lower panel. **b** Solid line: $\delta\langle r^4 \rangle^{A,A-2}$ values relative to $\delta\langle r^4 \rangle^{176,174} = 7$ fm⁴ (star) extracted from isotope shifts of the α_{PTB} transition using atomic theory. Dashed lines: *ab initio* nuclear theory predictions [1.8/2.0 (EM), VS1 and VS2; $\Delta\text{N}^2\text{LO}_{\text{GO}}$, VS1]. The estimated nuclear theory uncertainties (68% confidence interval) are given by the gray bands.

Nuclear structure effects

Recent developments have made heavy nuclei accessible to nuclear *ab initio* calculations [15, 33]. To predict $\delta\langle r^4 \rangle$, we use the valence-space in-medium similarity renormalization group (VS-IMSRG) [12, 13] together with

the quasi-particle vacua shell model (QVSM) [33] to solve the many-body Schrödinger equation. We employ nucleon-nucleon and three-nucleon interactions from chiral effective field theory, using the so-called 1.8/2.0 (EM) [34] and $\Delta\text{N}^2\text{LO}_{\text{GO}}$ [35] interactions, which differ in their construction and how they are fit to data, to give insight into interaction uncertainties. To assess many-body uncertainties, we solve the VS-IMSRG at the two- and three-body truncations [36] and employ two different valence spaces VS1 and VS2 in the QVSM (see Methods). In Fig. 2 **a**, we show the prediction of the nonlinearity from our nuclear structure calculations, where the uncertainty is represented by the gray band. The latter stems from a correlated statistical model taking into account interaction and many-body uncertainties including correlations between isotope pairs. The two sets of calculations using the 1.8/2.0 (EM) Hamiltonian with valence spaces VS1 and VS2 serve as representative samples of our nuclear theory predictions. Since the best-fit line is compatible with the *ab initio* calculations for $\delta\langle r^4 \rangle$, we assume $\delta\langle r^4 \rangle$ to be the leading King-plot nonlinearity in Yb.

Extracting nuclear deformation from atomic spectroscopy data

Combining isotope-shift measurements, nuclear mass-ratio measurements, and charge radius measurements [32] with atomic structure calculations of $G_\alpha^{(4)}$ (see Eq. (1)) using AMBiT [37], we recast the Yb King-plot analysis into a measurement of nuclear deformation, which can be used to benchmark nuclear structure calculations. The detailed procedure is illustrated in the Supplemental Material, and the extracted changes in $\delta\langle r^4 \rangle$ relative to the reference value of $\delta\langle r^4 \rangle^{176,174} = 7$ fm⁴ (star) are shown in Fig. 2 **b**. This reference value is selected based on input from both our *ab initio* results and density functional theory calculations [8] that all predict $\delta\langle r^4 \rangle^{176,174} = 6 - 8$ fm⁴. The experimental data show that the evolution of $\delta\langle r^4 \rangle^{A,A-2}$ along the isotope chain is nearly flat. This is remarkably consistent with our *ab initio* calculations within uncertainties.

Nonetheless, the linear fit in Fig. 2 **a** gives a 23σ preference for more than one nonlinearity, leaving open the possibility of a new boson being responsible for the next-to-leading King nonlinearity.

Bounds on new physics

To extract bounds on the hypothetical new boson, we combine our isotope shift measurements ($\nu_{\alpha_{\text{PTB}}}$, $\nu_{\gamma_{\text{PTB}}}$) and nuclear mass measurements with the Yb measurements reported by Ref. [30] (ν_δ). Using the generalized King-plot method [10], we can eliminate the King-plot nonlinearity induced by $\delta\langle r^4 \rangle$ from the system of isotope shift equations. We thereby set bounds on new

physics that are unaffected by the theoretical uncertainties, assuming that higher-order SM terms beyond the quartic shift are negligible.

Figure 3 shows the exclusion plot in the parameter plane of the new boson mass m_ϕ versus its coupling strength to electrons and neutrons, α_{NP} . The new bound provided by this work is shown in red. It supersedes the upper bounds from previous King-plot analyses in Ca^+ (cyan [38], blue [39]) and Yb^+ (black [8, 30]), excluding the parameter space shaded in orange. The inset in Fig. 3 shows the 2σ upper and lower bound (dotted red line) from our work. If the second King-plot nonlinearity were to be explained by new physics only, the couplings and mass of the new boson would be expected to reside between the 2σ upper bound (solid red line) and the 2σ lower bound (dotted red line), which are only distinguishable in this inset. Competing astrophysical and laboratory bounds are shown as exclusion regions and green dashed curves. A detailed discussion of the bounds can be found in the Supplementary Material.

Discussion and conclusion

We measured the isotope shifts for the $^2S_{1/2} \rightarrow ^2D_{5/2}$ electric quadrupole transition and the $^2S_{1/2} \rightarrow ^2F_{7/2}$ electric octupole transition on five stable, spinless Yb^+ isotopes and with relative uncertainties on the order of 10^{-8} to 10^{-9} , as well as mass ratios of these isotopes to a precision of 4×10^{-12} .

Our measurements, combined with atomic structure calculations, have enabled a first direct extraction of the evolution of $\delta\langle r^4 \rangle$ across the ytterbium isotope chain. To understand whether the change in the nuclear charge distribution is consistent with the strong interaction, we have performed *ab initio* calculations based on chiral effective field theory interactions. Our results reproduce the experimental $\delta\langle r^4 \rangle$ remarkably well for such heavy nuclei. This observable can provide direct insights into nuclear shapes from high-precision laser spectroscopy. An exciting future direction is to advance this work to the neutron-rich calcium isotopes. This can widen the search for the new boson and shed light on the puzzling increase of charge radii towards ^{52}Ca [52].

Our isotope-shift and nuclear mass measurements, combined with the isotope-shift measurements of Ref. [30], in combination with the generalized King plot method [10], allow us to set competitive spectroscopy bounds on new bosonic mediators between neutrons and electrons. With increasing experimental precision, data from more isotopes will be needed to overcome atomic and nuclear structure uncertainties. In ytterbium, a possible candidate is ^{166}Yb with a half-life of 54 hours, which would be feasible for high-precision laser spectroscopy and, given a sufficient sample size, also conceivable for mass spectrometry with the PENTATRAP setup. Another interesting option is to use elements Sn [53] or Xe [54], which each have seven spinless, stable isotopes and suitable clock transitions that could be found in the

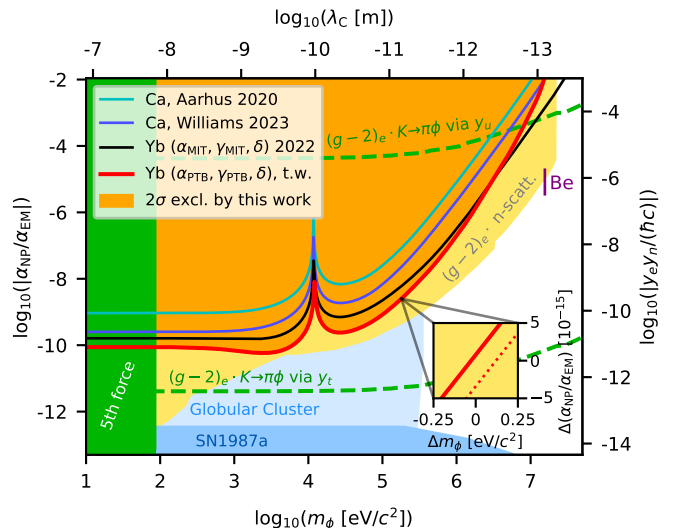


Fig. 3: Exclusion plot for the new boson ϕ coupling to electrons and neutrons. Solid lines: 2σ upper bounds from Ca^+ King plots (cyan: Aarhus [38], blue: Williams [39]), Yb^+ King plots (black: [8, 30]), and from this work (red) on the product of couplings $y_e y_n / (\hbar c) = 4\pi\alpha_{\text{NP}}$ to electrons and neutrons depending on the new boson’s mass m_ϕ and equivalently on the Compton wavelength $\lambda_C = \hbar / (m_\phi c)$. The inset shows an extract of the 2σ upper bound (solid red line) and the 2σ lower bound (dotted red line) produced by this work. The shaded areas are excluded by non-isotope-shift experiments: the constraint on y_e from $(g-2)_e$ [40, 41], times the constraints on y_n from neutron optics [42] and neutron scattering experiments [42–45] (yellow), fifth force searches [46, 47], the globular cluster [48, 49], and the supernova SN1987A [50]. The dashed curves show the constraint on y_e from $(g-2)_e$ times the constraint on y_n from $K \rightarrow \pi + \text{invisible}$ assuming the new boson ϕ couples only to the top-quark (via y_t) or only to the up-quark (via y_u). The purple band labeled “Be” indicates the coupling range required for a protophobic boson with $m_\phi = 17 \text{ MeV}/c^2$ to explain the ATOMKI anomaly [51].

different ionization stages [55]. These prospects suggest that isotope-shift spectroscopy may soon provide the strongest laboratory bounds on the new boson in the mass range of $m_\phi = 10^2 \text{ eV}/c^2 - 5 \times 10^7 \text{ eV}/c^2$.

Methods

Experimental treatment

The mass-ratio determinations to the precision presented rely on the use of highly charged ions to increase the cyclotron frequency. The highly charged $^A\text{Yb}^{42+}$ ions are produced in a room-temperature electron beam ion trap via in-trap laser ablation [56], allowing isotope selection via multiposition targets with isotope-enriched samples of YbO . A cloud of highly charged ions is extracted with

a kinetic energy of approximately $4\text{ keV}/q$ and transported through an electrostatic beamline equipped with a Bradbury-Nielsen Gate [57] for time-of-flight selection of a single charge state. The initial kinetic energy is reduced to a few eV/q via two pulsed drift tubes, one above the magnet and one right above the Penning-trap assembly inside the magnet. At this energy, the ions can be caught in the upper trap using a low-voltage potential-lift scheme.

Given the field strength of the superconducting magnet of about 7 T , the trap geometry, and the detection system's resonance frequencies, the eigenfrequencies of trapped ${}^A\text{Yb}^{42+}$ ions are approximately 26 MHz for the trap-modified cyclotron frequency, 700 kHz and 475 kHz for the axial frequencies, and 9.5 kHz and 4.3 kHz for the magnetron frequencies for trap 2 and 3, respectively.

The determination of eigenfrequencies is done via amplification of the image current using a resonant circuit near the axial frequency connected to one of the correction electrodes at each trap. To bring the resonant circuit in resonance with the axial frequency, it is tuned by means of a varicap (voltage controlled capacitance) [21]. This way the trap-potential settings can be kept identical for both measurement positions, assuring identical field imperfections for both ions and suppressed systematic shifts on the determined cyclotron frequency ratio. The radial eigenfrequencies are determined via sideband coupling and in case of the trap modified cyclotron frequency via the phase sensitive PnP method [58].

The cyclotron frequency $\nu_c = qB/(2\pi m)$ of an ytterbium ion with mass m and charge q in a magnetic field B is determined from all measured eigenfrequencies with $\nu_c^2 = \nu_+^2 + \nu_z^2 + \nu_-^2$ [20], with the magnetron frequency ν_- determined in the preparation of the measurement cycle with sufficient precision due to the frequency hierarchy and respective error propagation. Every subsequent cyclotron frequency measurement of the two ions yields a cyclotron frequency ratio. The ratio is calculated from interpolated values of the cyclotron frequency measurement of one ion species to the time-stamp of the other ion species to adjust to first-order magnetic field drifts.

With the measured R_A^{CF} the nuclear mass ratios are derived via

$$\eta_A = R_A^{\text{CF}} + \frac{(R_A^{\text{CF}} - 1) \left[28m_e - E_{172}^{(28)}/c^2 \right] - \Delta E_A^{(28)}/c^2}{m({}^{172}\text{Yb}) - 70m_e + E_{172}^{(70)}/c^2}. \quad (4)$$

Here, $m({}^{172}\text{Yb})$ [23] is the mass of the neutral atom and m_e [24] the electron mass. $E_{172}^{(28)}$ and $E_{172}^{(70)}$ are the binding energies of the 28 electrons in the ${}^{172}\text{Yb}^{42+}$ ion and 70 electrons in the ${}^{172}\text{Yb}$ atom, respectively. Thus, the denominator in Eq. (4) represents the nuclear mass of ${}^{172}\text{Yb}$, i.e., $m({}^{172}\text{Yb}^{70+})$, or m_{172} in the main text. The necessary electron binding energies and their dependence on isotopes $\Delta E_A^{(28)} = E_{172}^{(28)} - E_A^{(28)}$ are calculated with the GRASP2018 code [22] discussed in later sections.

The isotope-shift spectroscopy is performed on single trapped and laser-cooled ions in a segmented radio-frequency (rf) Paul trap [25, 26], operated at an rf frequency of $\Omega_{\text{rf}}/2\pi = 24.38\text{ MHz}$. The axial confinement is set by dc voltages supplied to the trapping segment and the neighboring segments. The axial and radial secular frequencies are around 200 kHz and 600 kHz , respectively. Micromotion is measured before and after each optical frequency ratio measurement using the photon correlation technique [59, 60].

The ion is cooled to approximately 0.6 mK , close to the Doppler temperature, on the dipole allowed ${}^2S_{1/2} \rightarrow {}^2P_{1/2}$ transition assisted by a repumper laser near 935 nm . Fluorescence from the decay of the ${}^2P_{1/2}$ state is collected by a lens of $N/A = 0.27$ [61] and imaged onto an electron-multiplying charge-coupled device camera. This enables state detection via the electron shelving technique. The ion is prepared in either the $|{}^2S_{1/2}, m_j = -1/2\rangle$ or the $|{}^2S_{1/2}, m_j = +1/2\rangle$ state using the $|{}^2S_{1/2}, m_j = +1/2\rangle \rightarrow |{}^2D_{5/2}, m_j = -3/2\rangle$ or the $|{}^2S_{1/2}, m_j = -1/2\rangle \rightarrow |{}^2D_{5/2}, m_j = +3/2\rangle$ transition assisted by a repumper laser near 1650 nm [62], respectively. Using a four-point servo lock, the probe lasers are locked to the Zeeman components of the transitions with opposite Zeeman sensitivities. To determine the center frequencies of the α and the γ transitions, we measure for about $3 \times 10^4\text{ s}$ and $4 \times 10^3\text{ s}$, respectively. Both spectroscopy lasers propagate along the same radial direction (y -axis). Both laser fields are frequency-shifted and pulsed using acousto-optic modulators.

To mitigate the influence of magnetic field fluctuations and noise, we actively stabilize the magnetic field by applying feedback in three dimensions via the current modulation of six auxiliary coils. We suppress coherent noise, stemming from the ac-mains at 50 Hz and harmonics, to $< 1\text{ nT}$ and incoherent noise up to a frequency of 550 Hz to $< 0.04\text{ nT}$ [63].

Theoretical treatment

The electron binding energies of highly charged ions and neutral Yb atoms defined in Eq. (4) are calculated via the *ab initio* fully relativistic multiconfiguration Dirac-Hartree-Fock (MCDHF) and relativistic configuration interaction (RCI) methods [64–66] implemented in the GRASP2018 code [22, 67]. Under this approach, the many-electron atomic state function is constructed as a linear combination of configuration state functions with common total angular momentum, magnetic, and parity quantum numbers. We first solve the MCDHF equations self-consistently [64–66] with the Dirac-Coulomb Hamiltonian. Then the RCI method is employed to calculate the contributions from mass shift, Breit interaction, frequency-dependent transverse photon interaction, and QED effects. Details of the calculations can be found in the Supplementary Material.

Making use of the precision of our nuclear mass measurements, we construct a set of quantities $\hat{\nu}_\tau^{a,r}$ (see

Eq. (J11)) that relate the isotope shifts of a given atomic transition τ and isotope pair a to the corresponding isotope shift in a reference isotope pair r . A set of transition-independent quantities $D^{a,r}$ can be computed from charge radius data [32], allowing us to determine and subtract the leading effect induced by a combination of the mass shift and the field shift. What remains is a new nuclear observable $Q^{a,r}$ (see Eq. (J15)), which quantifies the evolution of the next-to-leading nuclear effect along the isotope chain. Assuming this effect is described by $\delta\langle r^4 \rangle$, as suggested by the nonlinearity decomposition plot (see Figure 2), $Q^{a,r}$ allows us to determine all values $\delta\langle r^4 \rangle^a$ once $\delta\langle r^4 \rangle^r$ (the value of $\delta\langle r^4 \rangle$ for the reference isotope pair) is fixed.

The *ab initio* nuclear theory predictions for $\delta\langle r^4 \rangle$ are obtained via the valence-space IMSRG [12, 13], which solves the many-body Schrödinger equation for a given input Hamiltonian H via a unitary transformation to a block-diagonal form, $\bar{H} = UHU^\dagger$. The unitary transformation is formulated with respect to a reference state $|\Phi_0\rangle$ and can be efficiently approximated at the normal-ordered two-body level, the IMSRG(2). For the transformed Hamiltonian, the valence-space Hamiltonian is decoupled and subsequently diagonalized via large-scale diagonalization methods.

We employ two nuclear Hamiltonians with two- and three-nucleon interactions derived from chiral effective field theory [the 1.8/2.0 (EM) [34] and $\Delta N^2\text{LOGO}$ [35] Hamiltonians] to study the interaction uncertainty. We consider two valence spaces: VS1 with a ^{132}Sn core and an active valence space consisting of $1g_{7/2}$, $2d_{5/2}$, $2d_{3/2}$, $3s_{1/2}$, $1h_{11/2}$ proton orbitals and $2f_{7/2}$, $1h_{9/2}$, $1i_{13/2}$, $2f_{5/2}$, $3p_{3/2}$, $3p_{1/2}$ neutron orbitals; and VS2 with a ^{154}Gd core and an active valence space consisting of $2d_{3/2}$, $3s_{1/2}$, $1h_{11/2}$ proton orbitals and $1h_{9/2}$, $1i_{13/2}$, $2f_{5/2}$, $3p_{3/2}$, $3p_{1/2}$ neutron orbitals. The dimensions of the employed valence spaces in Yb isotopes are larger than 10^{11} , the current limit of standard shell model diagonalizations, so our results are only possible through the use of the scalable, systematically improvable QVSM [33]. To compute $\langle r^2 \rangle$ and $\langle r^4 \rangle$, we evaluate the ground-state expectation values of the translationally invariant point-proton radius operators r_p^2 and r_p^4 . For $\langle r^2 \rangle$, we also include the spin-orbit [68] and relativistic Darwin-Foldy [69] corrections and account for the finite size of nucleons. We employ a correlated statistical uncertainty model to assess uncertainties in our calculations. Errors due to many-body truncations in *ab initio* calculations are systematic in nature, producing similar errors in neighboring isotopes. As a result, strong correlations arise, which we account for. Details of the calculations and the statistical model are given in the Supplementary Material.

Acknowledgments

We thank Martin Steinel and Vladan Vuletić for helpful discussions.

This work is supported by the Max Planck Society (MPG), the International Max Planck Research Schools for Precision Tests of Fundamental Symmetries (IMPRS-PTFS), the European Research Council (ERC) under the European Union’s Horizon 2020 research and innovation programme under Grant Agreements 832848 (FunI) and 101020842 (EUSTRONG), and by the Deutsche Forschungsgemeinschaft (DFG, German Research Foundation) – Project-ID 273811115 – SFB 1225 ISOQUANT as well as under Germany’s Excellence Strategy – EXC-2123 QuantumFrontiers – 390837967 (RU B06) and through Grant No. CRC 1227 (DQ-mat, projects B02 and B03). This work has been supported by the Max-Planck-RIKEN-PTB-Center for Time, Constants, and Fundamental Symmetries. L.S.D. acknowledges support from the Alexander von Humboldt Foundation. This work comprises parts of the Ph.D. thesis work of M.D. to be submitted to Heidelberg University, Germany, parts of the Ph.D. thesis work of C.-H.Y. to be submitted to Leibniz Universität Hannover, Germany, and parts of the Ph.D. thesis work of M.H. to be submitted to the TU Darmstadt, Germany. M.H., T.M., and A.S. gratefully acknowledge the computing time provided on the high-performance computer Lichtenberg at the NHR Centers NHR4CES at TU Darmstadt. N.S. acknowledges the support of the “Program for promoting research on the supercomputer Fugaku”, MEXT, Japan (JPMXP1020230411), and the MCRP program of the Center for Computational Sciences, University of Tsukuba (NUCLSM). E.F. and F.K. thank CERN for their hospitality during the early phase of this work.

Author contributions

The experimental methods were developed by M.D., C.-H.Y., L.S.D., S.E., H.A.F., A.R., C.S., K.B., T.E.M. The experiment was performed by M.D., C.-H.Y., L.S.D., S.E., P.F., H.A.F., M.F., N.H. The data were analyzed by M.D., C.-H.Y., L.S.D., S.E., H.A.F., M.F., T.E.M. Atomic and nuclear structure calculations, and the theoretical interpretation were performed by M.H., F.K., C.L., T.M., J.C.B., J.B., E.F., G.G., Z.H., A.S., N.S. The manuscript was worked on by M.D., C.-H.Y., M.H., F.K., C.L., T.M., J.C.B., K.B., L.S.D., M.F., E.F., H.A.F., N.H., A.S., T.E.M. All authors discussed and approved the results as well as the manuscript.

Competing interests

The authors declare no competing interests.

Additional information

Correspondence and requests for materials should be addressed to Menno Door and Chih-Han Yeh.

References

- [1] Delaunay, C., *et al.*: Probing atomic Higgs-like forces at the precision frontier. *Phys. Rev. D* **96**, 093001 (2017) <https://doi.org/10.1103/PhysRevD.96.093001>
- [2] Frugiuele, C., *et al.*: Constraining new physics models with isotope shift spectroscopy. *Phys. Rev. D* **96**, 015011 (2017) <https://doi.org/10.1103/PhysRevD.96.015011>
- [3] Berengut, J.C., *et al.*: Probing new long-range interactions by isotope shift spectroscopy. *Phys. Rev. Lett.* **120**, 091801 (2018) <https://doi.org/10.1103/PhysRevLett.120.091801>
- [4] Safronova, M.S., *et al.*: Search for new physics with atoms and molecules. *Rev. Mod. Phys.* **90**, 025008 (2018) <https://doi.org/10.1103/RevModPhys.90.025008>
- [5] Rana, R., Höcker, M., Myers, E.G.: Atomic masses of strontium and ytterbium. *Phys. Rev. A* **86**, 050502 (2012) <https://doi.org/10.1103/PhysRevA.86.050502>
- [6] Counts, I., *et al.*: Evidence for nonlinear isotope shift in Yb^+ search for new boson. *Phys. Rev. Lett.* **125**, 123002 (2020) <https://doi.org/10.1103/PhysRevLett.125.123002>
- [7] Nesterenko, D.A., *et al.*: High-precision mass measurement of ^{168}Yb for verification of nonlinear isotope shift. *Int. J. Mass Spectrom.* **458**, 116435 (2020) <https://doi.org/10.1016/j.ijms.2020.116435>
- [8] Hur, J., *et al.*: Evidence of two-source King plot nonlinearity in spectroscopic search for new boson. *Phys. Rev. Lett.* **128**, 163201 (2022) <https://doi.org/10.1103/PhysRevLett.128.163201>
- [9] Repp, J., *et al.*: PENTATRAP: a novel cryogenic multi-Penning-trap experiment for high-precision mass measurements on highly charged ions. *Appl. Phys. B* **107**, 983 (2012) <https://doi.org/10.1007/s00340-011-4823-6>
- [10] Berengut, J.C., *et al.*: Generalized King linearity and new physics searches with isotope shifts. *Phys. Rev. Res.* **2**, 043444 (2020) <https://doi.org/10.1103/PhysRevResearch.2.043444>
- [11] Allehabi, S.O., *et al.*: Nuclear deformation as a source of the nonlinearity of the King plot in the Yb^+ ion. *Phys. Rev. A* **103**, 030801 (2021) <https://doi.org/10.1103/PhysRevA.103.L030801>
- [12] Hergert, H., *et al.*: The in-medium similarity renormalization group: a novel *ab initio* method for nuclei. *Phys. Rep.* **621**, 165 (2016) <https://doi.org/10.1016/j.physrep.2015.12.007>
- [13] Stroberg, S.R., *et al.*: Nonempirical interactions for the nuclear shell model: an update. *Ann. Rev. Nucl. Part. Sci.* **69**, 307 (2019) <https://doi.org/10.1146/annurev-nucl-101917-021120>
- [14] Hergert, H.: A guided tour of *ab initio* nuclear many-body theory. *Front. Phys.* **8**, 379 (2020) <https://doi.org/10.3389/fphy.2020.00379>
- [15] Miyagi, T., *et al.*: Converged *ab initio* calculations of heavy nuclei. *Phys. Rev. C* **105**, 014302 (2022) <https://doi.org/10.1103/PhysRevC.105.014302>
- [16] Epelbaum, E., Hammer, H.W., Meißner, U.G.: Modern theory of nuclear forces. *Rev. Mod. Phys.* **81**, 1773 (2009) <https://doi.org/10.1103/RevModPhys.81.1773>
- [17] King, W.H.: Comments on the article “Peculiarities of the isotope shift in the samarium spectrum”. *J. Opt. Soc. Am.* **53**, 638 (1963) <https://doi.org/10.1364/JOSA.53.000638>
- [18] Roux, C., *et al.*: The trap design of PENTATRAP. *Appl. Phys. B* **107**, 997 (2012) <https://doi.org/10.1007/s00340-011-4825-4>
- [19] Rischka, A., *et al.*: Mass-difference measurements on heavy nuclides with an eV/c^2 accuracy in the PENTATRAP spectrometer. *Phys. Rev. Lett.* **124**, 113001 (2020) <https://doi.org/10.1103/PhysRevLett.124.113001>
- [20] Brown, L.S., Gabrielse, G.: Precision spectroscopy of a charged particle in an imperfect Penning trap. *Phys. Rev. A* **25**, 2423 (1982) <https://doi.org/10.1103/PhysRevA.25.2423>
- [21] Heiße, F., *et al.*: High-precision measurement of the proton’s atomic mass. *Phys. Rev. Lett.* **119**, 033001 (2017) <https://doi.org/10.1103/PhysRevLett.119.033001>
- [22] Froese Fischer, C., *et al.*: GRASP2018 – a Fortran 95 version of the general relativistic atomic structure package. *Comput. Phys. Commun.* **237**, 184 (2019) <https://doi.org/10.1016/j.cpc.2018.10.032>
- [23] Huang, W.J., *et al.*: The AME 2020 atomic mass evaluation (I). evaluation of input data, and adjustment procedures. *Chinese Phys. C* **45**, 030002 (2021) <https://doi.org/10.1088/1674-1137/abddb0>
- [24] Tiesinga, E., *et al.*: CODATA recommended values

- of the fundamental physical constants: 2018. Rev. Mod. Phys. **93**, 025010 (2021) <https://doi.org/10.1103/RevModPhys.93.025010>
- [25] Pyka, K., *et al.*: A high-precision segmented Paul trap with minimized micromotion for an optical multiple-ion clock. Appl. Phys. B **114**, 231 (2014) <https://doi.org/10.1007/s00340-013-5580-5>
- [26] Keller, J., *et al.*: Probing time dilation in Coulomb crystals in a high-precision ion trap. Phys. Rev. Appl. **11**, 011002 (2019) <https://doi.org/10.1103/PhysRevApplied.11.011002>
- [27] Matei, D.G., *et al.*: 1.5 μm lasers with sub-10 mHz linewidth. Phys. Rev. Lett. **118**, 263202 (2017) <https://doi.org/10.1103/PhysRevLett.118.263202>
- [28] Lange, R., *et al.*: Lifetime of the $^2F_{7/2}$ level in Yb^+ for spontaneous emission of electric octupole radiation. Phys. Rev. Lett. **127**, 213001 (2021) <https://doi.org/10.1103/PhysRevLett.127.213001>
- [29] Lange, R., *et al.*: Improved limits for violations of local position invariance from atomic clock comparisons. Phys. Rev. Lett. **126**, 011102 (2021) <https://doi.org/10.1103/PhysRevLett.126.011102>
- [30] Ono, K., *et al.*: Observation of nonlinearity of generalized King plot in the search for new boson. Phys. Rev. X **12**, 021033 (2022) <https://doi.org/10.1103/PhysRevX.12.021033>
- [31] Figueroa, N.L., *et al.*: Precision determination of isotope shifts in ytterbium and implications for new physics. Phys. Rev. Lett. **128**, 073001 (2022) <https://doi.org/10.1103/PhysRevLett.128.073001>
- [32] Angeli, I., Marinova, K.P.: Table of experimental nuclear ground state charge radii: an update. At. Data Nucl. Data Tables **99**, 69 (2013) <https://doi.org/10.1016/j.adt.2011.12.006>
- [33] Shimizu, N., *et al.*: Variational approach with the superposition of the symmetry-restored quasiparticle vacua for nuclear shell-model calculations. Phys. Rev. C **103**, 014312 (2021) <https://doi.org/10.1103/PhysRevC.103.014312>
- [34] Hebeler, K., *et al.*: Improved nuclear matter calculations from chiral low-momentum interactions. Phys. Rev. C **83**, 031301 (2011) <https://doi.org/10.1103/PhysRevC.83.031301>
- [35] Jiang, W.G., *et al.*: Accurate bulk properties of nuclei from $A = 2$ to ∞ from potentials with Δ isobars. Phys. Rev. C **102**, 054301 (2020) <https://doi.org/10.1103/PhysRevC.102.054301>
- [36] Heinz, M., *et al.*: In-medium similarity renormalization group with three-body operators. Phys. Rev. C **103**, 044318 (2021) <https://doi.org/10.1103/PhysRevC.103.044318>
- [37] Kahl, E.V., Berengut, J.C.: AMBiT: A program for high-precision relativistic atomic structure calculations. Comput. Phys. Commun. **238**, 232 (2019) <https://doi.org/10.1016/j.cpc.2018.12.014>
- [38] Solaro, C., *et al.*: Improved isotope-shift-based bounds on bosons beyond the standard model through measurements of the $^2D_{3/2} - ^2D_{5/2}$ interval in Ca^+ . Phys. Rev. Lett. **125**, 123003 (2020) <https://doi.org/10.1103/PhysRevLett.125.123003>
- [39] Chang, T.T., *et al.*: New limit on isotope-shift-based bounds for beyond standard model light bosons via King's linearity in Ca^+ . arXiv (2023) <https://doi.org/10.48550/arXiv.2311.17337>
- [40] Hanneke, D., Fogwell, S., Gabrielse, G.: New measurement of the electron magnetic moment and the fine structure constant. Phys. Rev. Lett. **100**, 120801 (2008) <https://doi.org/10.1103/PhysRevLett.100.120801>
- [41] Fan, X., *et al.*: Measurement of the electron magnetic moment. Phys. Rev. Lett. **130**, 071801 (2023) <https://doi.org/10.1103/PhysRevLett.130.071801>
- [42] Leeb, H., Schmiedmayer, J.: Constraint on hypothetical light interacting bosons from low-energy neutron experiments. Phys. Rev. Lett. **68**, 1472 (1992) <https://doi.org/10.1103/PhysRevLett.68.1472>
- [43] Nesvizhevsky, V.V., Pignol, G., Protasov, K.V.: Neutron scattering and extra short range interactions. Phys. Rev. D **77**, 034020 (2008) <https://doi.org/10.1103/PhysRevD.77.034020>
- [44] Pokotilovski, Y.N.: Constraints on new interactions from neutron scattering experiments. Phys. Atom. Nucl. **69**, 924 (2006) <https://doi.org/10.1134/S1063778806060020>
- [45] Barbieri, R., Ericson, T.E.O.: Evidence against the existence of a low mass scalar boson from neutron-nucleus scattering. Phys. Lett. B **57**, 270 (1975) [https://doi.org/10.1016/0370-2693\(75\)90073-8](https://doi.org/10.1016/0370-2693(75)90073-8)
- [46] Bordag, M., Mohideen, U., Mostepanenko, V.M.: New developments in the Casimir effect. Phys. Rep. **353**, 1 (2001) [https://doi.org/10.1016/S0370-1573\(01\)00015-1](https://doi.org/10.1016/S0370-1573(01)00015-1)
- [47] Bordag, M., *et al.*: Advances in the Casimir Effect. Oxford University Press, Oxford

- (2009). <https://doi.org/10.1093/acprof:oso/9780199238743.001.0001>
- [48] Grifols, J.A., Masso, E.: Constraints on finite range baryonic and leptonic forces from stellar evolution. *Phys. Lett. B* **173**, 237 (1986) [https://doi.org/10.1016/0370-2693\(86\)90509-5](https://doi.org/10.1016/0370-2693(86)90509-5)
- [49] Grifols, J.A., Masso, E., Peris, S.: Energy loss from the sun and red giants: Bounds on short range baryonic and leptonic forces. *Mod. Phys. Lett. A* **4**, 311 (1989) <https://doi.org/10.1142/S0217732389000381>
- [50] Raffelt, G.: Limits on a CP-violating scalar axion-nucleon interaction. *Phys. Rev. D* **86**, 015001 (2012) <https://doi.org/10.1103/PhysRevD.86.015001>
- [51] Krasznahorkay, A.J., *et al.*: Observation of anomalous internal pair creation in ^8Be : A possible indication of a light, neutral boson. *Phys. Rev. Lett.* **116**, 042501 (2016) <https://doi.org/10.1103/PhysRevLett.116.042501>
- [52] Garcia Ruiz, R.F., *et al.*: Unexpectedly large charge radii of neutron-rich calcium isotopes. *Nat. Phys.* **12**, 594 (2016) <https://doi.org/10.1038/nphys3645>
- [53] Leibbrandt, D.R., *et al.*: Prospects of a thousand-ion Sn^{2+} Coulomb-crystal clock with sub- 10^{-19} inaccuracy. *arXiv* (2022) <https://doi.org/10.48550/arXiv.2205.15484>
- [54] Rehbehn, N.-H., *et al.*: Narrow and ultranarrow transitions in highly charged Xe ions as probes of fifth forces. *Phys. Rev. Lett.* **131**, 161803 (2023) <https://doi.org/10.1103/PhysRevLett.131.161803>
- [55] Lyu, C., Keitel, C.H., Harman, Z.: Ultrastable optical, XUV and soft-x-ray clock transitions in open-shell highly charged ions. *arXiv* (2023) <https://doi.org/10.48550/arXiv.2305.09603>
- [56] Schweiger, C., *et al.*: Production of highly charged ions of rare species by laser-induced desorption inside an electron beam ion trap. *Rev. Sci. Instrum.* **90**, 123201 (2019) <https://doi.org/10.1063/1.5128331>
- [57] Bradbury, N.E., Nielsen, R.A.: Absolute values of the electron mobility in hydrogen. *Phys. Rev.* **49**, 388 (1936) <https://doi.org/10.1103/PhysRev.49.388>
- [58] Cornell, E.A., *et al.*: Mode coupling in a Penning trap: π pulses and a classical avoided crossing. *Phys. Rev. A* **41**, 312 (1990) <https://doi.org/10.1103/PhysRevA.41.312>
- [59] Berkeland, D.J., *et al.*: Minimization of ion micro-motion in a Paul trap. *J. Appl. Phys.* **83**, 5025 (1998) <https://doi.org/10.1063/1.367318>
- [60] Keller, J., *et al.*: Precise determination of micro-motion for trapped-ion optical clocks. *J. Appl. Phys.* **118**, 104501 (2015) <https://doi.org/10.1063/1.4930037>
- [61] Pyka, K.: High-precision ion trap for spectroscopy of Coulomb crystals. PhD thesis, Leibniz Universität Hannover, Hanover, Germany (2013). <https://doi.org/10.15488/8143>
- [62] Roos, C.F., *et al.*: ‘Designer atoms’ for quantum metrology. *Nature* **443**, 316 (2006) <https://doi.org/10.1038/nature05101>
- [63] Fürst, H.A., *et al.*: Coherent excitation of the highly forbidden electric octupole transition in $^{172}\text{Yb}^+$. *Phys. Rev. Lett.* **125**, 163001 (2020) <https://doi.org/10.1103/PhysRevLett.125.163001>
- [64] Grant, I.P.: Relativistic calculation of atomic structures. *Adv. Phys.* **19**, 747 (1970) <https://doi.org/10.1080/00018737000101191>
- [65] Desclaux, J.P., Mayers, D.F., O’Brien, F.: Relativistic atomic wave functions. *J. Phys. B: Atom. Mol. Phys.* **4**, 631 (1971) <https://doi.org/10.1088/0022-3700/4/5/004>
- [66] Grant, I.P.: *Relativistic Quantum Theory of Atoms and Molecules: Theory and Computation*. Springer, New York (2007). <https://doi.org/10.1007/978-0-387-35069-1>
- [67] Jönsson, P., *et al.*: An introduction to relativistic theory as implemented in GRASP. *Atoms* **11**, 7 (2023) <https://doi.org/10.3390/atoms11010007>
- [68] Ong, A., Berengut, J.C., Flambaum, V.V.: The Effect of spin-orbit nuclear charge density corrections due to the anomalous magnetic moment on halonuclei. *Phys. Rev. C* **82**, 014320 (2010) <https://doi.org/10.1103/PhysRevC.82.014320>
- [69] Friar, J.L., Martorell, J., Sprung, D.W.L.: Nuclear sizes and the isotope shift. *Phys. Rev. A* **56**, 4579 (1997) <https://doi.org/10.1103/PhysRevA.56.4579>
- [70] Schüssler, R.X., *et al.*: Detection of metastable electronic states by Penning trap mass spectrometry. *Nature* **581**, 42 (2020) <https://doi.org/10.1038/s41586-020-2221-0>

- [71] Filianin, P., *et al.*: Direct Q -value determination of the β^- decay of ^{187}Re . *Phys. Rev. Lett.* **127**, 072502 (2021) <https://doi.org/10.1103/PhysRevLett.127.072502>
- [72] Kromer, K., *et al.*: High-precision mass measurement of doubly magic ^{208}Pb . *Eur. Phys. J. A* **58**, 202 (2022) <https://doi.org/10.1140/epja/s10050-022-00860-1>
- [73] Kromer, K., *et al.*: Atomic mass determination of uranium-238. *Phys. Rev. C* **109**, 021301 (2024) <https://doi.org/10.1103/PhysRevC.109.L021301>
- [74] Wineland, D.J., Dehmelt, H.G.: Principles of the stored ion calorimeter. *J. Appl. Phys.* **46**, 919 (1975) <https://doi.org/10.1063/1.321602>
- [75] Cornell, E.A., *et al.*: Single-ion cyclotron resonance measurement of $M(\text{CO}^+)/M(\text{N}_2^+)$. *Phys. Rev. Lett.* **63**, 1674–1677 (1989) <https://doi.org/10.1103/PhysRevLett.63.1674>
- [76] Brown, L.S., Gabrielse, G.: Geonium theory: Physics of a single electron or ion in a Penning trap. *Rev. Mod. Phys.* **58**, 233 (1986) <https://doi.org/10.1103/RevModPhys.58.233>
- [77] Ketter, J., *et al.*: First-order perturbative calculation of the frequency-shifts caused by static cylindrically-symmetric electric and magnetic imperfections of a penning trap. *Int. J. Mass Spectrom.* **358**, 1 (2014) <https://doi.org/10.1016/j.ijms.2013.10.005>
- [78] Van Dyck, R.S., *et al.*: Number dependency in the compensated Penning trap. *Phys. Rev. A* **40**, 6308 (1989) <https://doi.org/10.1103/PhysRevA.40.6308>
- [79] Schuh, M., *et al.*: Image charge shift in high-precision Penning traps. *Phys. Rev. A* **100**, 023411 (2019) <https://doi.org/10.1103/PhysRevA.100.023411>
- [80] Rau, S., *et al.*: Penning trap mass measurements of the deuteron and the HD^+ molecular ion. *Nature* **585**, 43 (2020) <https://doi.org/10.1038/s41586-020-2628-7>
- [81] Kramida, A., *et al.*: NIST atomic spectra database (version 5.9) (2021) <https://doi.org/10.18434/T4W30F>
- [82] Malyshev, A.V., *et al.*: QED calculation of the ground-state energy of berylliumlike ions. *Phys. Rev. A* **90**, 062517 (2014) <https://doi.org/10.1103/PhysRevA.90.062517>
- [83] Malyshev, A.V., *et al.*: Ab initio calculations of energy levels in Be-like xenon: Strong interference between electron-correlation and QED effects. *Phys. Rev. Lett.* **126**, 183001 (2021) <https://doi.org/10.1103/PhysRevLett.126.183001>
- [84] Jönsson, P., *et al.*: GRASP manual for users. *Atoms* **11**, 68 (2023) <https://doi.org/10.3390/atoms11040068>
- [85] Lyu, C., *et al.*: Extreme field calculations for Penning ion traps and corresponding strong laser field scenarios. *Mol. Phys.*, 2252105 (2023) <https://doi.org/10.1080/00268976.2023.2252105>
- [86] Recommended Values of Standard Frequencies for Applications Including the Practical Realization of the Metre and Secondary Representations of the Definition of the Second
- [87] Beaty, E.C.: Simple electrodes for quadrupole ion traps. *J. Appl. Phys.* **61**, 2118 (1987) <https://doi.org/10.1063/1.337968>
- [88] Keller, J., *et al.*: Simple vibration-insensitive cavity for laser stabilization at the 10^{-16} level. *Appl. Phys. B* **116**, 203 (2014) <https://doi.org/10.1007/s00340-013-5676-y>
- [89] Yeh, C.-H., *et al.*: Robust and scalable rf spectroscopy in first-order magnetic sensitive states at second-long coherence time. *New J. Phys.* **25**, 093054 (2023) <https://doi.org/10.1088/1367-2630/acfc14>
- [90] Tan, T.R., *et al.*: Precision characterization of the $^2D_{5/2}$ state and the quadratic Zeeman coefficient in $^{171}\text{Yb}^+$. *Phys. Rev. A* **104**, 010802 (2021) <https://doi.org/10.1103/PhysRevA.104.L010802>
- [91] Lange, R., *et al.*: Coherent suppression of tensor frequency shifts through magnetic field rotation. *Phys. Rev. Lett.* **125**, 143201 (2020) <https://doi.org/10.1103/PhysRevLett.125.143201>
- [92] Huntemann, N., *et al.*: Single-ion atomic clock with 3×10^{-18} systematic uncertainty. *Phys. Rev. Lett.* **116**, 063001 (2016) <https://doi.org/10.1103/PhysRevLett.116.063001>
- [93] Peik, E., Schneider, T., Tamm, C.: Laser frequency stabilization to a single ion. *J. Phys. B: At. Mol. Opt. Phys.* **39**, 145 (2005) <https://doi.org/10.1088/0953-4075/39/1/012>
- [94] Lindvall, T., *et al.*: Noise-induced servo errors in optical clocks utilizing rabi interrogation. *Metrologia* **60**, 045008 (2023) <https://doi.org/10.1088/1681-7575/acdfd4>
- [95] Sanner, C., *et al.*: Optical clock comparison for

- Lorentz symmetry testing. *Nature* **567**, 204 (2019) <https://doi.org/10.1038/s41586-019-0972-2>
- [96] Tsukiyama, K., Bogner, S.K., Schwenk, A.: In-medium similarity renormalization group for nuclei. *Phys. Rev. Lett.* **106**, 222502 (2011) <https://doi.org/10.1103/PhysRevLett.106.222502>
- [97] Entem, D.R., Machleidt, R.: Accurate charge dependent nucleon nucleon potential at fourth order of chiral perturbation theory. *Phys. Rev. C* **68**, 041001 (2003) <https://doi.org/10.1103/PhysRevC.68.041001>
- [98] Simonis, J., *et al.*: Saturation with chiral interactions and consequences for finite nuclei. *Phys. Rev. C* **96**, 014303 (2017) <https://doi.org/10.1103/PhysRevC.96.014303>
- [99] Stroberg, S.R., *et al.*: *Ab Initio* limits of atomic nuclei. *Phys. Rev. Lett.* **126**, 022501 (2021) <https://doi.org/10.1103/PhysRevLett.126.022501>
- [100] Hebeler, K.: Three-nucleon forces: Implementation and applications to atomic nuclei and dense matter. *Phys. Rep.* **890**, 1 (2021) <https://doi.org/10.1016/j.physrep.2020.08.009>
- [101] Arthuis, P., Hebeler, K., Schwenk, A.: Neutron-rich nuclei and neutron skins from chiral low-resolution interactions. *arXiv* (2024) <https://doi.org/10.48550/arXiv.2401.06675>
- [102] Bogdanovich, P., Žukauskas, G.: Approximate allowance for superposition of configurations in atomic spectra. *Sov. Phys. Collect.* **23**, 13 (1983)
- [103] Kozlov, M.G., Porsev, S.G., Flambaum, V.V.: Manifestation of the nuclear anapole moment in the M1 transitions in bismuth. *J. Phys. B: At. Mol. Opt. Phys.* **29**, 689 (1996) <https://doi.org/10.1088/0953-4075/29/4/011>
- [104] Kozlov, M.G., *et al.*: Combination of perturbation theory with the configuration-interaction method. *Phys. Rev. A* **105**, 052805 (2022) <https://doi.org/10.1103/PhysRevA.105.052805>
- [105] Delaunay, C., *et al.*: Probing new spin-independent interactions through precision spectroscopy in atoms with few electrons. *Phys. Rev. D* **96**, 115002 (2017) <https://doi.org/10.1103/PhysRevD.96.115002>
- [106] Blum, K., Kushnir, D.: Neutrino signal of collapse-induced thermonuclear supernovae: the case for prompt black hole formation in SN1987A. *Astrophys. J.* **828**, 31 (2016) <https://doi.org/10.3847/0004-637X/828/1/31>
- [107] Knapen, S., Lin, T., Zurek, K.M.: Light dark matter: Models and constraints. *Phys. Rev. D* **96**, 115021 (2017) <https://doi.org/10.1103/PhysRevD.96.115021>

Appendix A Experimental setup for the mass-ratio determinations

The experimental setup PENTATRAP as well as the measurement schemes and techniques, are similar to those in prior measurements. Details can be found in [9, 18, 70–73] and just a short overview and details of this measurement are given.

The cryogenic setup with a stack of five identical Penning traps is placed in a superconducting magnet with a field strength of 7 T. The traps and detection electronics, see Fig. A1, are cooled to the temperature of liquid helium (4 K) providing a low noise environment for ion detection and cooling. The ions are loaded with deliberate low transport efficiency to load only a single ion per shot into the trap tower. Traps 2 and 3 are used simultaneously as measurement traps which increases statistics and allows for cross-checks of trap and detection system related systematic shifts. The determination of the cyclotron frequencies of two ions is done sequentially. To switch ion species in the measurement traps the set of ions is adiabatically transported to the neighboring traps, see positions 1 and 2 in Fig. A1.

The axial eigenmotion is resistively cooled via the detection system: The induced image current by an ion creates a voltage drop across the high impedance of the connected superconducting resonance circuit (LCR). This voltage signal acts as negative feedback dampening the ion’s axial motion, limited by the thermal noise of the detection systems at approximately 4.2 K. Radial modes are indirectly cooled by energy exchange to the axial mode by sideband coupling through a quadrupolar RF field [58]. The supposedly single ions are cleaned from possible contaminant ions by using broadband magnetron excitation with simultaneous magnetron sideband cooling of the ion of interest and trap potential variation. Following this procedure, a set of three ions is prepared in an $A-A'-A$ sequence in the three central traps, and these are reloaded on average every second day due to charge exchange with rest gas atoms.

For the measurement of the axial frequencies, the dip method is applied [74]. Because of the difference in charge-to-mass ratio, the axial frequencies of different isotopes in the same charge state, stored at the same trapping potential, are separated by multiple kHz. This difference is bridged by tuning the resonance frequency of the LCR circuit using varicaps (varactor diodes), see Fig. A1. Compared to adjusting the trap potential to tune the axial frequency on a fixed detection system resonance, this reduces systematic uncertainties on R_A^{CF} caused by field imperfections [19]. For the radial modes the double-dip method is used and for the precise determination of the trap-modified cyclotron frequency, the phase-sensitive Rabi-type Pulse and Phase (PnP) technique [75] is applied. The initial phase imprint for the

PnP method is realized by dipolar excitation of the trap-modified cyclotron mode, increasing its amplitude ρ_+ on the order of 12 μm . This is followed by a free evolution of the phase and finally coupling of the radial and axial modes to measure the evolved phase using the axial detection system. A reference phase at a short phase evolution time is subtracted from the long evolution time phase to cancel phase offsets in the measurement chain. The equality of excitation radii for the different ions has been tested to a level of 2%, which ensures a low impact of systematic shifts dependent on the excitation radii on the final cyclotron frequency ratio. During the long phase evolution time, the dip spectrum is recorded, resulting in a simultaneous determination of the two higher eigenfrequencies. The ion species is switched inside both measurement traps by transporting the three ions up or down via potential variation, with one ion always in one of the two storage traps 1 or 4.

At the beginning of each measurement cycle, all eigenfrequencies are determined roughly via dip and double-dip methods for both types of ions to determine measurement settings for the PnP method and tune the detection system on resonance with the axial frequencies. The automated measurement cycle is split into two parts: The trap-modified cyclotron frequency is determined via multiple PnP-type phase measurements with a set of up to 10 different evolution times between 0.1 and 100 s, each phase measurement repeated for 4 to 6 times, allowing to unwrap the absolute frequency. In the second part, typically running for 12 hours before repeating the absolute frequency determination, only the shortest and longest of these evolution times are measured to follow the change of the trap-modified cyclotron frequency due to changes in the magnetic field. This is possible due to our liquid helium level and pressure-stabilized superconducting magnet, resulting in a shot-to-shot ν_+ frequency stability on the level of $3 - 5 \times 10^{-11}$. During these 12 hours, the ion species is switched between 20 and 30 times in each trap.

For maximal relative precision (highest possible cyclotron frequency), we used one of the highest charge states of 42+ produced by our ion source. The eigenfrequencies in PENTATRAP’s Penning traps (defined by the magnetic field strength and the resonance frequency of the detection system) are approximately $\nu_+ \approx 26$ MHz, $\nu_z \approx 470 - 700$ kHz and $\nu_- \approx 5 - 10$ kHz, for the modified cyclotron, axial and magnetron frequency respectively. A summary of all trapping parameters is given in Table A1.

With the binding energies presented, the neutral masses of the isotopes can also be calculated. The resulting uncertainty is limited by the literature value for $m(^{172}\text{Yb})$ with a relative uncertainty of 8×10^{-11} . All neutral masses are given in Tab. A2 and are compared to the current literature values of the atomic mass evaluation 2020 [23]. The masses of three isotopes agree within 1.5σ and the mass of ^{168}Yb shows a deviation by 3.5σ . The uncertainty of $m(^{168}\text{Yb})$ is improved compared to the literature value by a factor of 7.

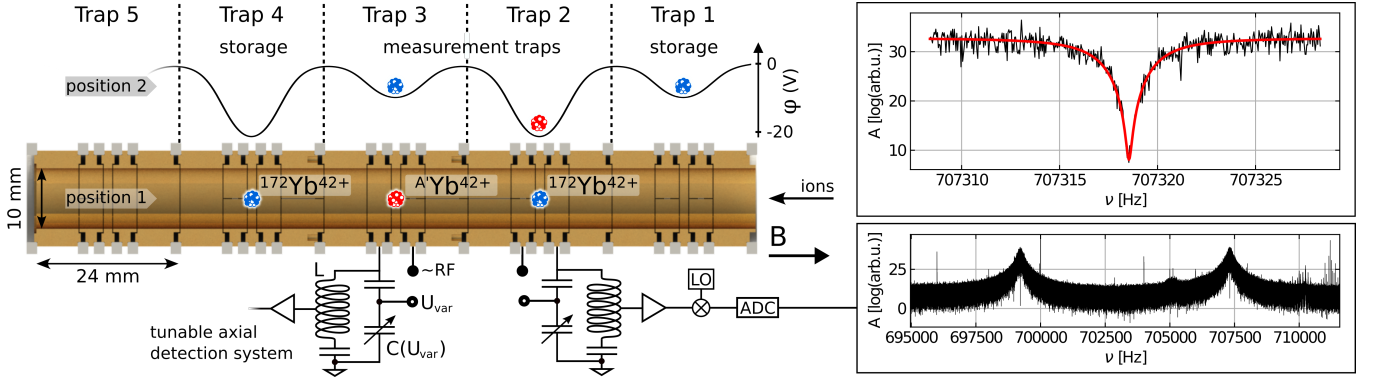


Fig. A1: Overview of the PENTATRAP measurement setup with a sectional view of the trap tower, approximate schematics of the detection system, and example spectra of the axial detection in trap 2 for the determination of the cyclotron frequency ratio of $^{176}\text{Yb}^{42+}$ over $^{172}\text{Yb}^{42+}$. The lower spectrum shows the detection system resonance frequency tuned to match one of the two axial frequencies of the respective ion during the measurement in position 1 and position 2. The upper spectrum shows a zoom-in of one axial dip spectrum of $^{172}\text{Yb}^{42+}$ with the model fit given as a red line.

Table A1: Trap parameters relevant in the analysis of the systematic effects. The approximate eigenfrequencies are given for the common reference ion $^{172}\text{Yb}^{42+}$. The magnetic field was calculated using the cyclotron frequency ν_c and ion's charge-to-mass ratio from literature [23].

Parameter	Trap 2	Trap 3
r_0 (mm) [18]	5.000 (5)	5.000 (5)
TR (1)	0.87966 (15)	0.87902 (7)
U_0 (V)	-28.14	-12.85
T_z (K)	5 (2)	8 (2)
$\rho_{+,exc}$ (μm)	12 (2)	12 (2)
RLC Q -factor (1)	≈ 3300	≈ 9800
ν_+ (MHz)	≈ 26.26	≈ 26.27
ν_z (kHz)	≈ 707.3	≈ 478.1
ν_- (kHz)	≈ 9.5	≈ 4.4
B_0 (T)	7.002 15 (2)	7.002 16 (2)
B_2 ($\frac{\text{mT}}{\text{m}^2}$)	28 (2)	-5 (2)
c_2 (10^{-3}mm^{-2})	-14.88576(1)	-14.89708(1)
c_4/c_2 (10^{-5}mm^{-2})	-3 (8)	-7 (8)
c_6/c_2 (10^{-6}mm^{-4})	-4 (6)	-2 (6)

Table A2: Neutral masses in atomic mass units of the five even Ytterbium isotopes determined from the measured cyclotron frequency ratios $R_A^{\text{CF}} = \nu_{c,172}/\nu_{c,A}$, the binding energy to of the 42 missing electrons $E_{172}^{(70)} - E_{172}^{(28)}$ and the literature mass of isotope $m(^{172}\text{Yb})$ [23]. For comparison also the literature mass values listed in the atomic mass evaluation 2020 [23].

Isotope A	$m(A)$ (this work)	$m(A)$ [23]
168	167.933 890 939 (14)	167.933 891 297 (100)
170	169.934 767 218 (14)	169.934 767 242 (11)
174	173.938 867 541 (14)	173.938 867 545 (11)
176	175.942 574 697 (14)	175.942 574 706 (15)

Appendix B Systematic effects and analysis of the mass ratio measurement data

A summary of all systematic shifts on the determined ratios can be found in Tab. B3 for both traps and the different mass ratios. Some of the given shifts are commonly known shifts and uncertainties on the real motional frequencies. Among these are the relativistic shift [76], shifts due to field imperfections [76, 77], and the image charge shift [78, 79]. The trap parameters necessary to calculate these and other effects are given in Tab. A1. The necessary dipole excitation for the phase imprint on the trap-modified cyclotron motion for the PnP technique was compared between two isotopes to check for equally increased amplitudes ρ_+ of this radial mode and yielded a maximum deviation of 2%. Although the absolute excitation radius cannot be determined with such precision, the precision of the excitation radius ratio allows for a significant reduction in systematic uncertainties. The uncertainty of the image charge shift effect originates from the most precise test to date of the respective analytical estimation of this effect, which agreed to a level of 5% limited by the experimental uncertainty [79]. In addition to these, there are systematic uncertainties mainly originating from our detection system and measurement methods. The highest uncertainty originates in the determination of the axial frequency via the dip determination, which is sensitive to the precision with which the resonance circuit can be tuned to the axial frequency [80]. The determination of the resonance frequency is precise to only 2 Hz in our setup. The given uncertainties on the determined ratio due to this effect are extracted from measurements of the axial frequency in dependence on the resonance frequency as well as full ratio determinations with deliberate detuning of the RLC resonance by

Table B3: Systematic corrections ΔR for the determined ratio $R^{\text{CF}} = R' + \Delta R$ with $R' = \nu_{c,172}/\nu_{c,A}$ being the measured ratio. All values are expressed in parts per trillion ($1 \cdot 10^{-12}$). For more details see text.

Effect	A	Trap 2	Trap 3
Field imperfect (B_i, c_i)	all	0.0 (0.5)	0.0 (0.5)
Nonlinear phase readout	all	0.0 (1.0)	0.0 (1.5)
Magnetron frequency	all	0.0 (1.0)	0.0 (1.0)
Dip lineshape	all	0.0 (4.0)	0.0 (5.0)
<hr/>			
Common total	all	0.0 (4.4)	0.0 (5.3)
<hr/>			
Image charge shift	176	-10.0 (0.5)	
	174	- 4.9 (0.2)	
	170	4.8 (0.2)	
	168	9.5 (0.5)	
<hr/>			
Special relativity	176	1.0 (1.5)	
	174	0.5 (1.5)	
	170	-0.5 (1.5)	
	168	-1.0 (1.5)	

10-20 Hz for only one ion. The nonlinear phase readout originates from a nonlinear transfer function of the ions cyclotron phase at the time of the PnP coupling pulse to the axial mode. The residual of the ideally linear transfer function follows a sinusoidal behavior with amplitudes of 0.25 and 0.5 degrees in trap 2 and 3, respectively. These phase offsets average out for the long accumulation time measurement, but create constant offsets for the short reference phase, which results in the given uncertainties. The magnetron frequency systematic uncertainty originates from the calculation of the magnetron frequencies of one ion from the measured magnetron frequency of the other, using the literature mass values. This is sufficient, since the cyclotron frequency ratio is more sensitive to the magnetron frequency difference than to the absolute value, which is only determined to low precision before each measurement.

All systematic shifts are corrected in the weighted mean cyclotron frequency ratio results of the individual traps. None of the dominant systematic shifts and uncertainties are correlated between the two measurement traps. The final value is determined from the weighted mean of the results of the two traps.

Appendix C *Ab initio* binding energy calculations for mass-ratio correction

The electron binding energies of neutral Yb and Ni-like Yb^{42+} can be obtained by summing the ionization potentials (IPs) of all the charge states listed in the NIST atomic database [81]. This results in the values 382, 457(614) and 350, 722(233) eV for the binding energies of the 70 and 28 electrons, respectively. To reduce uncertainties in these values, advanced atomic structure

calculations were performed in this work. The procedure is straightforward for the case of highly charged Yb^{42+} . However, for neutral Yb, many close-lying levels render it difficult to treat the electron correlations accurately. Nevertheless, considering that the IPs of Yb and Yb^+ are experimentally known to be 6.254160(12) eV and 12.179185(25) eV [81], respectively, we can partially avoid this problem by calculating the binding energy of Yb^{2+} .

The calculations were performed via the *ab initio* fully relativistic multiconfiguration Dirac-Hartree-Fock (MCDHF) and relativistic configuration interaction (RCI) methods [64–66] implemented in the GRASP2018 code [22, 67]. The many-electron atomic state function (ASF) is constructed as a linear combination of configuration state functions (CSFs) with common total angular momentum (J), magnetic (M), and parity (P) quantum numbers: $|\Gamma P J M\rangle = \sum_k c_k |\gamma_k P J M\rangle$. Each CSF $|\gamma_k P J M\rangle$ is built from products of one-electron orbitals (Slater determinants), jj -coupled to the appropriate angular symmetry and parity, and γ_k represents orbital occupations, together with orbital and intermediate quantum numbers necessary to uniquely define the CSF. Γ collectively denotes all the γ_k involved in the representation of the ASF. c_k is the corresponding mixing coefficient. We first solve the MCDHF equations self-consistently [64–66] under the Dirac-Coulomb Hamiltonian, to obtain an ASF, represented by the set of c_k , together with the set of radial orbitals. Then the RCI method is employed to calculate the contributions from mass shift (or nuclear recoil effect), Breit interaction, frequency-dependent transverse photon interaction, and QED effects.

The ground state of $^{172}\text{Yb}^{42+}$ is described by the configuration $[\text{Ar}]3d^{10} 1S_0$. In the single-configuration Dirac-Hartree-Fock calculation, one obtains a binding energy of 351379.33 eV for a point-like nuclear charge. The corresponding mass shift equals $-0.87(5)$ eV with the uncertainty of the order of $(m_e/M)(\alpha Z)^4 m_e c^2$ (M is the mass of the nucleus). The Fermi model for nuclear-charge distribution gives rise to a correction of $-45.06(8)$ eV due to the finite nuclear size effect, with the uncertainty resulting from the nuclear radius predictions. The Breit interaction further contributes energy of -367.66 eV, and the frequency-dependent transverse-photon interaction adds 6.65 eV to the total binding energy. The residual Coulomb-Breit interaction, the so-called correlation energy, is significant as well but more complicated to account for. Thus, its contribution and uncertainty will be discussed in detail in later paragraphs. Similar calculations were also performed for neutral ^{172}Yb , with the corresponding values being summarized in Tab. C4.

Furthermore, the QED effects are implemented in the GRASP2018 package via a screened-hydrogen-like model for vacuum polarization (VP) and self-energy (SE) contributions, respectively [66]. With values of -54.61 eV and 307.45 eV for the VP and SE corrections, respectively, they reduce the binding energy by 252.84 eV for

Table C4: Different contributions to the total binding energies of $^{172}\text{Yb}^{42+}$ and $^{172}\text{Yb}^{2+}$: DHF₀, the DHF energy assuming a point-like nuclear charge; MS, the mass shift; FNS, the finite nuclear size effect; Breit, the frequency-independent transverse photon interaction; ωTP , the frequency-dependent transverse photon interaction; QED, the QED contribution based on screened-hydrogenic model; SDc, the correlation energies arising from single and double electron substitutions; HOc, the systematic effect from all unaccounted correlation effects. The values of the DHF₀, Breit, ωTP , and SDc terms are basis dependent. After taking into account all correlation effects, the basis dependency will be resolved. Thus, their uncertainties are accounted for as a whole in the high-order correlation energy (HOc). The total binding energies are rounded up to integer numbers. All entries are shown in units of eV.

Ion	Ground state	DHF ₀	MS	FNS	Breit	ωTP	QED	SDc	HOc	Total
$^{172}\text{Yb}^{42+}$	[Ar]3d ¹⁰ 1S ₀	351379.33	-0.87 (3)	-45.06 (8)	-367.66	6.65	249.4 (3.5)	48.76 (1)	1.4 (1.4)	350773 (5)
$^{172}\text{Yb}^{2+}$	[Xe]4f ¹⁴ 1S ₀	382828.68	-0.90 (3)	-45.31 (8)	-384.95	6.79	251.1 (3.5)	117.26 (9)	12 (12)	382283 (16)

the case of $^{172}\text{Yb}^{42+}$. By comparing these values with respect to the results obtained from a hydrogen-like model without screening, we find that the many-electron QED effects contribute of the order of -15.65 eV. The uncertainty of these QED calculations can be inferred from *ab initio* QED calculations in Be-like Xe⁵⁰⁺ and U⁸⁸⁺ with a sub-eV uncertainty [82, 83]. We find that the results obtained by the GRASP2018 code equal 99.03 eV and 625.02 eV, respectively, for the two Be-like ions, and they are larger by 0.85 eV and 8.61 eV, respectively, compared to the *ab initio* QED results [82, 83]. Assuming a similar systematic error, we obtain a QED contribution of $-249.4(3.5)$ eV to the total binding energy of $^{172}\text{Yb}^{42+}$. However, since QED effects are significant mainly for inner-shell electrons, a similar QED correction of $-251.1(3.5)$ eV is obtained for the case of $^{176}\text{Yb}^{2+}$.

To derive the electron correlation energy, we systematically expand the size of the CSF basis set by allowing single and double (SD) substitutions of electrons from the occupied orbitals of the ground-state configuration to the systematically increasing set of correlation orbitals. These correlation orbitals are added and optimized layer-by-layer [84] up to $n = 10$ (n is the principle quantum number), with the highest orbital angular momentum in each layer equals $n - 1$. It is found that the increment of the correlation energy at each layer decreases exponentially as a function of n [85]. This allows us to extrapolate the electron correlation energy to $n = \infty$. With this scheme, we obtain an SD correlation energy of 48.76(1) eV and 117.26(9) eV for $^{172}\text{Yb}^{42+}$ and $^{172}\text{Yb}^{2+}$, respectively. The uncertainties are derived from extrapolations based on different numbers of data points.

Nevertheless, the full binding energy contains correlations from electron exchanges beyond the SD substitution scheme, as well as from basis functions outside the model space. These contributions are difficult to evaluate but can be estimated from the ionization potentials (IPs) of low-charged ions. We found that, based on SD substitutions from the 4s orbital, the calculated IPs for Yb, Yb⁺, and Yb²⁺ are 0.80 eV, 0.40 eV, and 0.65 eV smaller than the experimental values (we note that the SD substitutions from orbitals below the 4s orbital generate more than 5 million CSFs for Yb⁺ and Yb³⁺, which

is beyond the capacity of available computing power at our disposal). As a conservative estimation (taken here as the difference between calculated and experimental values, as discussed above), one can assume that the average shift of the calculated IPs for ions from Yb²⁺ to Yb²³⁺ will not be larger than 0.8 eV. To cover this effect, we add a shift of 8.8(8.8) eV to the correlation-energy difference between Yb²⁺ and Yb²⁴⁺. Since this shift is obtained based on the SD substitution from the 4s orbital, for the total-binding-energy calculations based on SD substitution from the 1s orbital, one has to add another 1.0(1.0) eV shift to account for the contributions from core-core and core-valence correlations. Furthermore, the average shifts due to electron correlations in the theoretical IPs for ions between Yb²⁴⁺ and Yb⁴¹⁺ can be constrained based on the calculations of Pd-like Xe⁸⁺ and Cu-like Kr⁷⁺, respectively. Since the QED effects are negligible for the IPs of Xe⁸⁺ and Kr⁷⁺, the discrepancy between experimental and calculated values arises from the unaccounted correlation effects. With SD substitutions from the 1s orbital, we arrive at an upper limit of 0.1 eV [72] for the average shift in IPs. Thus, a shift of 0.9(9) eV has to be added to the correlation-energy difference between Yb²⁴⁺ and Yb⁴²⁺. To be conservative, we also assume an average of 0.1 eV correlation-energy shift in the IPs for ions with charge states higher than Yb⁴²⁺. In total, the unaccounted high-order correlation effects are derived to be 1.4(1.4) eV and 12(12) eV for Yb⁴²⁺ and Yb²⁺, respectively.

Therefore, electron correlation effects contribute 50.2(1.4) eV and 129(12) eV to the total binding energy of Yb⁴²⁺ and Yb²⁺, respectively. Altogether, we obtain $E_{172}^{(28)} = 350,773(5)$ eV and $E_{172}^{(68)} = 382,283(16)$ eV, where we have round up the numbers to integer values of eV. Adding up the IPs of the outermost two electrons, one arrives at $E_{172}^{(70)} = 382.301(16)$ eV for the total binding energy of the neutral atom. These results agree with the values obtained from the NIST atomic database but with the uncertainties reduced by more than 2 orders of magnitude.

Since each Yb isotope bears a different mass and nuclear size, its total binding energy entails isotope shifts arising from different nuclear recoil and field effects.

To investigate the isotope dependence of $\Delta E_A^{(28)}$, see Eq. 4, we start with a Dirac-Hartree-Fock (DHF) and RCI calculation where only the ground state configuration is considered for each isotope and charge state. With $^{172}\text{Yb}^{42+}$ as a reference, we obtain $\Delta E_A^{(28)} = -0.50(1)$ eV, $-0.25(1)$ eV, $0.25(1)$ eV, and $0.50(1)$ eV for isotopes $A = 168, 170, 174$ and 176 , respectively.

Appendix D Experimental details for frequency measurements

We determined the isotope shifts from absolute frequencies $\nu_{\alpha,\gamma}^A$ of the $^2S_{1/2} \rightarrow ^2D_{5/2}$ electric quadrupole (α) and the $^2S_{1/2} \rightarrow ^2F_{7/2}$ electric octupole (γ) transitions in the stable even isotopes of $^A\text{Yb}^+$ ($A \in \{168, 170, 172, 174, 176\}$). For this, we measured the optical frequency ratios $\mathcal{R}_{\alpha,\gamma} = \nu_{\alpha,\gamma}^A / \nu_{\gamma}^{171}$ with ν_{γ}^{171} corresponding to the frequency of the γ transition between the $F = 0$ and $F = 3$ hyperfine states of the $^{171}\text{Yb}^+$ isotope [29]. We determined the absolute frequencies by multiplying \mathcal{R} to the recommended frequency value $\nu_{\gamma}^{171} = 642121496772645.12(12)$ Hz [86] and correcting for systematic frequency shifts.

The experimental setup is sketched in Fig. D2. Two separate experiments are involved in the \mathcal{R} measurements, one is based on a segmented linear radio-frequency (rf) Paul trap [25, 26], which is used to trap even isotopes of Yb^+ , and the other one is based on a ring style rf Paul trap [87] trapping $^{171}\text{Yb}^+$. Two stable laser systems are employed for probing the α and the γ transitions. A laser at 822 nm is frequency-doubled to interrogate the α transition near 411 nm in the even isotopes. This laser is stabilized to an ultra-low expansion (ULE) optical cavity, obtaining short-term frequency stability of 5×10^{-16} at 10 s averaging time [88]. The larger frequency shifts between the isotopes are bridged with an electro-optic modulator (EOM) in the infrared, while smaller frequency shifts are applied with a double-pass acousto-optic modulator (AOM) in the blue.

A stable laser at 934 nm is frequency-doubled to 467 nm and continuously steered to be on resonance with the γ transition of the $^{171}\text{Yb}^+$ isotope [29]. Part of the infrared light is frequency offset via an EOM and used to stabilize the frequency of a second laser at 934 nm. The frequency-doubled output of this laser is used for the interrogation of the γ transitions in the even isotopes. In both setups, the short-term frequency stability of the lasers is improved by locking to a cryogenic silicon cavity [27]. A frequency comb setup is used to perform the optical frequency ratio measurements.

In the segmented, linear rf Paul trap setup used for the even isotopes, the quantization axis is defined by a static magnetic field of about 65 μT oriented in the xz -plane at an angle of $\beta = 26.8(4.0)^\circ$ with respect to

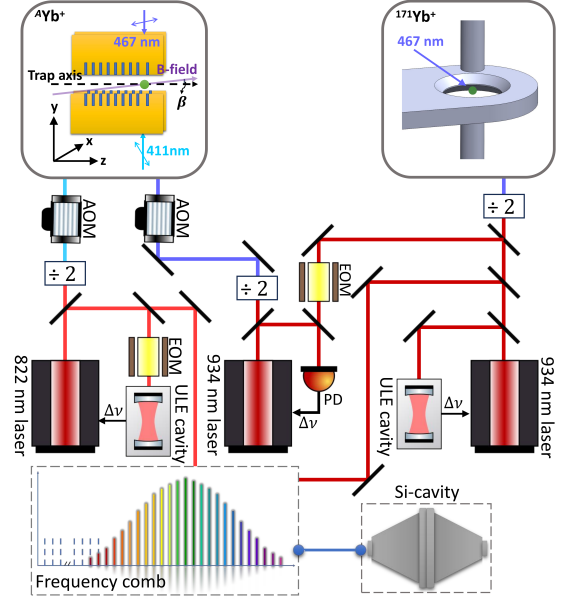


Fig. D2: Simplified schematic representation of the experimental setup used for the interrogation of the α and the γ transitions near 411 nm and 467 nm, respectively. Even isotopes of Yb^+ are trapped in a segmented linear radio-frequency (rf) Paul trap [25, 26] and the odd isotope $^{171}\text{Yb}^+$ is trapped in a ring style rf Paul trap [87]. Probe lasers in the infrared are referenced to ultra-low expansion (ULE) optical cavities for short-term stability, then further stabilized to a cryogenic silicon cavity [27]. Electro-optic modulators (EOMs) are used to bridge the isotope frequency differences and acousto-optic modulators (AOMs) are used to fine-tune the laser frequencies. A frequency comb setup is used to perform the optical frequency ratio measurements.

the trap axis z (shown in Fig. 1 a), obtained from geometric measurements. The lasers to interrogate the α and the γ transitions are aligned in the radial trapping direction y . Since the electronic states of the even Yb^+ isotopes do not contain sublevels with zero magnetic moment $m = 0$, the α and γ transitions are first-order magnetic-field sensitive. We employ active magnetic field stabilization [63, 89] to increase the maximum coherent interrogation time for these transitions.

AOMs are used to address pairs of Zeeman components with opposite magnetic field sensitivity and the center transition frequencies are obtained via averaging in post-processing. For the α and the γ transition, the $|^2S_{1/2}, m_J = \pm 1/2\rangle \rightarrow |^2D_{5/2}, m_J = \pm 5/2\rangle$ and the $|^2S_{1/2}, m_J = \pm 1/2\rangle \rightarrow |^2F_{7/2}, m_J = \pm 1/2\rangle$ transitions are interrogated, respectively.

The basic interrogation sequence starts with 5 ms of laser cooling via the $^2S_{1/2} \rightarrow ^2P_{1/2}$ electric dipole transition near 370 nm, assisted by laser light near 935 nm for repumping via the $^2D_{3/2} \rightarrow ^3[3/2]_{1/2}$ transition. It is followed by state preparation to either of the $|^2S_{1/2}, m_J = \pm 1/2\rangle$ Zeeman sublevels via the $|^2S_{1/2}, m_J = \mp 1/2\rangle \rightarrow$

$|^2D_{5/2}, m_J = \pm 3/2\rangle$ transitions, assisted by the $^2D_{5/2} \rightarrow ^2P_{3/2}$ transition near 1650 nm [62]. A Rabi pulse of $t_\pi = 2.1$ ms ($t_\pi = \pi/\Omega_R$, where Ω_R is the Rabi frequency) or of about 50 ms is employed to interrogate the α or the γ transition. The maximum excitation probability is $P_\alpha = 45\%$ and $P_\gamma = 80\%$ for the α and the γ transitions. After this, laser light near 370 nm is applied for 2.5 ms for state-selective fluorescence detection. Successful excitation results in the absence of fluorescence. After state detection, repumpers near wavelengths of 638 nm and 1650 nm for the $^2F_{7/2} \rightarrow ^1[5/2]_{5/2}$ and the $^2D_{5/2} \rightarrow ^2P_{3/2}$ transitions, respectively, are switched on to return the ion to the cooling cycle. A valid experimental cycle requires the detection of fluorescence after repumping.

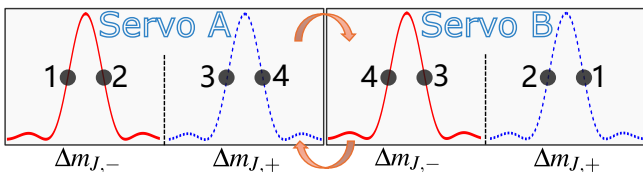


Fig. D3: Schematic representation of the four-point servo lock used to determine the transition frequencies. The solid (red) and dashed (blue) curves correspond to the spectra of the $\Delta m_{J,\mp} : |^2S_{1/2}, m_J = \mp 1/2\rangle \rightarrow |^2D_{5/2}, m_J = \mp 5/2\rangle$ or the $\Delta m_{J,\mp} : |^2S_{1/2}, m_J = \pm 1/2\rangle \rightarrow |^2F_{7/2}, m_J = \pm 1/2\rangle$ transitions, respectively. The numbers denote the order of the interrogation frequencies. “Servo A” and “Servo B” are performed in an interleaved manner.

This interrogation sequence is continuously repeated with 50 cycles at each point of a four-point servo lock. Here, the servo points run over fixed positive and negative detunings from each component of the Zeeman pair, as illustrated in Fig. D3. After interrogating at all four points, the mean AOM frequency is updated to obtain the same excitation probability for equal positive and negative detunings. The γ transition is additionally interrogated at a lower laser intensity using an independent servo. From the high- and low-intensity servos, the transition frequency that is free from probe light-induced ac-Stark shift is derived via linear extrapolation.

Appendix E Systematic and statistical uncertainties for the frequency measurements

For each of the two transitions in the even isotopes, one systematic frequency shift dominates and causes most of the systematic uncertainty. The electric quadrupole shift stemming from the interaction of the quadrupole moment with the electric field gradient at the ion

position dominates for the α transition. The electric quadrupole shift can be calculated from the electric field gradient, the electric quadrupole moment, and the angle β between the symmetry axis of the gradient and the applied magnetic field. The electric field gradient is determined to be $dE_z/dz = 3.1610(15)$ V/mm² from an axial secular frequency of $\nu_{\text{ax}} = 211.97(5)$ kHz. A potential electric field gradient of 0.2 V/mm² from stray electric fields is added in quadrature to the uncertainty of dE_z/dz . With the electric quadrupole moment of $12.5(4) ea_0^2$ [90], we obtain an electric quadrupole shift of $-9.3(1.8)$ Hz. For the γ transition, this systematic shift is negligible due to a more than 400 times smaller quadrupole moment [91].

The dominant systematic effect for the γ transition is the probe-light induced ac-Stark shift. Even though Rabi excitation at two different laser intensities is employed to determine the transition frequency free from the ac-Stark shift, imperfect light path design caused the beam pointing to change with the rf power applied to the AOM. This shift effect is estimated by comparing the slope of the extrapolation to zero ac-Stark shift during the measurement campaign to that of a measurement where the change in the probe light power is realized independent of the AOM power. From the comparison, a maximum shift of $-9.2(11.1)$ Hz is determined. In contrast, for the α transition, the probe-light induced ac-Stark shift even with a shorter pulse duration of $t_\pi = 2.1$ ms is calculated from the differential polarizability in Ref. [63] and causes a negligible shift of only $2(1)$ mHz.

In addition to the major systematic shifts discussed so far, Tab. E5 includes smaller shift effects and their uncertainties. These shift effects will be discussed in the following.

The ion is confined with radial secular frequencies of about 600 kHz and an axial secular frequency of around 200 kHz and laser-cooled to the Lamb-Dicke regime reaching a temperature of $0.60(6)$ mK. Minimization and measurements of the excess micromotion (EMM) using the photon correlation technique [60] were performed only before and after the measurement campaign. Based on these measurements, we estimate the mean rf field causing EMM to be $\{E_x, E_y, E_z\} = \{100(500), 100(500), 150(50)\}$ V/m. Here, the uncertainties are set to the maximum variations seen over the three months prior to the measurements. Both effects from uncompensated EMM and intrinsic micromotion due to the finite ion temperature are considered to calculate the second-order Doppler shift and the second-order Stark shift. The corresponding second-order Doppler shift is calculated as $-0.002(4)$ Hz and the second-order Stark shift is $-0.015(47)$ Hz and $-0.003(10)$ Hz for the α and the γ transition, respectively. The involved static differential polarizability for the α transition is found in Ref. [63] and for the γ transition in Ref. [92].

The blackbody radiation shift is calculated to be $-0.26(13)$ Hz for the α transition and $-0.046(1)$ Hz for the γ transition considering thermal radiation with an

Table E5: Leading systematic shifts $\delta\nu_\alpha$, $\delta\nu_\gamma$ and corresponding uncertainties $u_{B,\alpha}$, $u_{B,\gamma}$ of the ${}^2S_{1/2} \rightarrow {}^2D_{5/2}$ electric quadrupole (α) and the ${}^2S_{1/2} \rightarrow {}^2F_{7/2}$ electric octupole (γ) transition for all even isotopes.

Systematic shift	$\delta\nu_\alpha$ [Hz]	$u_{B,\alpha}$ [Hz]	$\delta\nu_\gamma$ [Hz]	$u_{B,\gamma}$ [Hz]
Electric quadrupole shift	-9.3	1.8	-0.016	0.003
Probe-light induced ac-Stark shift	0.002	0.001	-9.2	11.1
Second-order Doppler shift	-0.002	0.004	-0.002	0.004
Second-order Stark shift	-0.015	0.047	-0.003	0.010
Blackbody radiation shift	-0.26	0.13	-0.045	0.001
Servo error induced shift	-	0.8	-	0.1
Total	-9.6	2.0	-9.3	11.1

effective temperature of $T_C = 297.1(1.4)$ K perturbing the ion [63, 92]. The temperature uncertainty assumed the maximum temperature difference measured at the chamber and the ion trap during the measurement campaign.

Magnetic field variations can cause servo errors because of the long dead time and non-randomized four-point servo lock sequence [93, 94]. These are estimated to be 0.8 Hz and 0.1 Hz for the measurements of the α and the γ transitions. By adding the uncertainties of the systematic shifts in quadrature, we determine the total systematic uncertainty for the α and the γ transition frequencies to be $u_{B,\alpha} = 2.0$ Hz and $u_{B,\gamma} = 11.1$ Hz, respectively.

The systematic uncertainty for the realization of the γ transition in ${}^{171}\text{Yb}^+$ has been evaluated to 1.7 mHz [95]. For the frequency ratio measurements, a gravitational redshift between the experimental setups for the even isotopes of Yb^+ and the ${}^{171}\text{Yb}^+$ of $-3.26(4) \times 10^{-17}$ has been taken into account.

The statistical uncertainties u_A from the measurements are listed in Tab. E6. The values correspond to the last point in the Allan deviation σ_y of the transition frequency measurements. Examples are shown in Fig. E4 for $\mathcal{R}_{\alpha,\gamma}$ of the α and the γ transitions in ${}^{168}\text{Yb}^+$. The fit to the Allan deviation for the α transition frequency measurement yields $\sigma_{\text{fit},\alpha} = 101.7(1.5) \text{ Hz}/\sqrt{\tau}$, and that of the Allan deviation for the γ transition is $\sigma_{\text{fit},\gamma} = 13.36(7) \text{ Hz}/\sqrt{\tau}$. Both of the fits agree with the instability expected from quantum projection noise.

Table E6: Statistical uncertainties $u_{A,\alpha}$, $u_{A,\gamma}$ for determining the α and the γ transition frequencies.

Isotope A	$u_{A,\alpha}$ [Hz]	$u_{A,\gamma}$ [Hz]
168	2.7	0.4
170	3.6	0.2
172	1.8	0.3
174	3.5	0.3
176	1.3	0.3

The total uncertainties of the transition frequencies for each isotope are given by $\sigma\nu_k = \sqrt{u_{A,k}^2 + u_{B,k}^2}$, with $k = \alpha, \gamma$. We determine the absolute frequencies of the α and the γ transitions for all five stable even isotopes

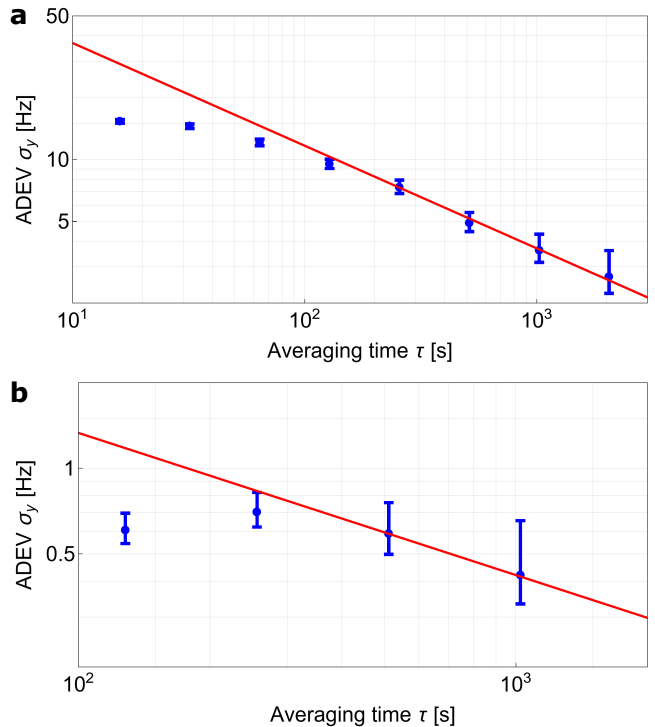


Fig. E4: Allan deviations σ_y of the α (a) and the γ (b) transition frequency measurements in ${}^{168}\text{Yb}^+$. The fits to the data yield $\sigma_{\text{fit},\alpha} = 101.7(1.5) \text{ Hz}/\sqrt{\tau}$ and $\sigma_{\text{fit},\gamma} = 13.36(7) \text{ Hz}/\sqrt{\tau}$, agreeing with the instabilities expected from quantum projection noise.

of Yb^+ with the frequency ratios, the literature value for the absolute frequency of the γ transition in ${}^{171}\text{Yb}^+$ [86], and the systematic shifts. Values are shown in Tab. E7. For determining the isotope shifts, we do not consider any common mode rejection and take into account the full uncertainties as given in Tab. E7.

Table E7: Absolute frequencies $\nu_{\alpha,\gamma}$ of the α and the γ transitions for all five stable even isotopes of Yb^+ .

Isotope A	$\nu_\alpha - 729 \text{ THz}$ [Hz]	$\nu_\gamma - 642 \text{ THz}$ [Hz]
168	481 090 977 315.9 (3.4)	108 197 800 720.0 (11.1)
170	478 911 878 447.9 (4.1)	112 635 960 391.1 (11.1)
172	476 867 027 166.9 (2.7)	116 785 150 892.3 (11.1)
174	475 283 963 017.6 (4.0)	119 917 471 350.4 (11.1)
176	473 774 909 821.9 (2.4)	122 893 863 395.6 (11.1)

Appendix F King plot analysis

From the King plot shown in Fig. 1 **b,c**, we can extract the slope and offset, which correspond to the constants $F_{\gamma\alpha}$ and $K_{\gamma\alpha}$ in Eq. (2), which result in $-2.22131(5)$ and $0.033363(8)$ Hz, respectively. We also resolve deviations from linearity on the average of $20.17(2)$ kHz. From the extracted slope, the nuclear mass-ratio uncertainties can be translated into frequency uncertainties. Here, the maximum translated frequency uncertainty is around 0.3 Hz, stemming from the (168, 170) isotope pair, improving on the 28 Hz uncertainty in Ref. [8].

Appendix G Nonlinearity decomposition

Table G8: Notation and references for the transitions used in the King plot analysis and the nonlinearity decomposition plot. “t.w.” abbreviates “this work”.

Notation	Transition	λ [nm]	Refs.
$\alpha_{\text{MIT}}, \alpha_{\text{PTB}}$	$^2S_{1/2} \rightarrow ^2D_{5/2}$ E2 in Yb ⁺	411	[6, 8], t.w.
β	$^2S_{1/2} \rightarrow ^2D_{3/2}$ E2 in Yb ⁺	435	[6]
$\gamma_{\text{MIT}}, \gamma_{\text{PTB}}$	$^2S_{1/2} \rightarrow ^2F_{7/2}$ E3 in Yb ⁺	467	[6, 8], t.w.
δ	$^1S_0 \rightarrow ^3P_0$ in Yb	578	[30]
ϵ	$^1S_0 \rightarrow ^1D_2$ in Yb	361	[31]

Given n isotope pairs, $n - 2$ King plot nonlinearities can be resolved by projecting the isotope shift data on n n -vectors. For simplicity, we use the same reference transition δ for all King plots entering our nonlinearity analysis and choose our basis in such a way that two basis vectors, $\check{\nu}_\delta$ and $\mathbf{1}$ (see Eq. (2)), lie within the plane of King linearity, whereas the other two, $\mathbf{\Lambda}_+ \propto (\check{\nu}_\delta^c - \check{\nu}_\delta^b, \check{\nu}_\delta^a - \check{\nu}_\delta^d, \check{\nu}_\delta^d - \check{\nu}_\delta^a, \check{\nu}_\delta^b - \check{\nu}_\delta^c)$ and $\mathbf{\Lambda}_- \propto (\check{\nu}_\delta^d - \check{\nu}_\delta^b, \check{\nu}_\delta^a - \check{\nu}_\delta^c, \check{\nu}_\delta^b - \check{\nu}_\delta^d, \check{\nu}_\delta^c - \check{\nu}_\delta^a)$, normalized to 1 Hz and with $a = (168, 170)$, $b = (170, 172)$, $c = (172, 174)$, $d = (174, 176)$, are orthogonal to this plane and directly calculable from the experimental data. In this way, we can use the same basis for the nonlinearity decomposition of the experimental data and for the *ab initio* predictions. The coordinates $(\lambda_+^{(\tau)}, \lambda_-^{(\tau)})$, $\tau \in \{\alpha_{\text{PTB}}, \alpha_{\text{MIT}}, \beta, \gamma_{\text{PTB}}, \gamma_{\text{MIT}}, \delta, \epsilon\}$, defined via Eq. (3), characterize the nonlinearities in the isotope shift ν_τ .

In the presence of one dominant source of King nonlinearity, the electronic coefficients $G^{(2)}, G^{(4)}, D, \dots$ (see Eq. (1)) drop out of the ratio $\lambda_-^{(\tau)}/\lambda_+^{(\tau)} = \lambda_-/\lambda_+$, making λ_-/λ_+ a transition-independent quantity. This motivates a linear fit through the origin of the (λ_+, λ_-) plane to the six data points $(\lambda_+^{(\tau)}, \lambda_-^{(\tau)})$ derived for the six transitions listed in Tab. G8. Indeed, the tension of the Yb isotope shift data for King linearity can be drastically reduced by introducing a King nonlinearity satisfying $\lambda_-/\lambda_+ = -1.777(14)$, leaving a residual nonlinearity at the level of 23σ .

We compare this slope to predictions of individual nonlinearity terms in Eq. (1) to identify the leading King plot nonlinearity. The new physics prediction for λ_-/λ_+ follows straightforwardly from Eqs. (1) and (3), and has a relative uncertainty of approximately 3×10^{-7} . The λ_-/λ_+ slope corresponding to the quadratic field shift $\delta\langle r^2 \rangle^2$ (see Eq. (1), dotted line in Fig. 2) can be derived from experimental data for $\delta\langle r^2 \rangle$ [32] with a relative uncertainty of approximately 2%. If the new physics (quadratic field shift) term were to dominate the nonlinearity, the experimental data points would be expected to lie on the dash-dotted (dotted) line in Fig. 2 **a**. We conclude that neither the new physics term nor the quadratic field shift term can be the dominant nonlinearity in the ytterbium King plot (Figure 1 **b,c**).

Our *ab initio* calculations of $\delta\langle r^4 \rangle$ fit better to data: In Figure 2 we show the projections of our chiral effective field theory calculations using the 1.8/2.0 (EM) interactions with valence spaces VS1 (dashed, blue) and VS2 (dashed, orange). Both agree within uncertainties (the 68% confidence interval is given by the gray band) with the linear fit to data, suggesting that $\delta\langle r^4 \rangle$ can explain the leading King nonlinearity in ytterbium. Our *ab initio* calculations are discussed in more detail in Appendix H.

Appendix H *Ab initio* nuclear structure calculations

The ground-state properties of atomic nuclei, such as $\langle r^2 \rangle$ and $\langle r^4 \rangle$, can be computed *ab initio* using effective field theories for the strong interactions between nucleons and systematically improvable many-body methods to solve the many-body Schrödinger equation. Yb isotopes are challenging to describe *ab initio* due to being heavy and open-shell, and our work leverages recent developments improving the treatment of three-nucleon forces in heavy nuclei [15] and performing large-scale diagonalizations of the many-body Hamiltonian [33].

Our calculations are performed with the valence-space IMSRG [12, 13, 96], which solves the many-body Schrödinger equation for a given input Hamiltonian H via a unitary transformation to a block-diagonal form, $\overline{H} = UHU^\dagger$. The unitary transformation $U = e^\Omega$ is formulated with respect to a reference state $|\Phi_0\rangle$ for the system of interest and can as a result be efficiently approximated at the normal-ordered two-body level, the IMSRG(2). We solve the IMSRG(2) in a model space of 15 oscillator shells based on an underlying harmonic oscillator basis with frequency $\hbar\omega = 12$ MeV, including three-nucleon forces with a truncation of $E_{3\text{max}} = 28$ made possible by Ref. [15]. For the transformed Hamiltonian, an effective valence-space Hamiltonian is decoupled and subsequently diagonalized via large-scale shell-model methods.

We employ two nuclear Hamiltonians with two- and three-nucleon interactions derived within chiral effective

field theory (EFT). The 1.8/2.0 (EM) Hamiltonian [34] is constructed from the $N^3\text{LO}$ nucleon-nucleon potential of Entem and Machleidt (EM) [97], transformed using the similarity renormalization group to a resolution scale of $\lambda = 1.8\text{ fm}^{-1}$, and $N^2\text{LO}$ three-nucleon interactions with a regulator cutoff $\Lambda_{3N} = 2.0\text{ fm}^{-1}$. It is fit to few-body systems (up to ${}^4\text{He}$) and predicts ground-state energies, spectra, and differential radius trends well in medium-mass and heavy nuclei [98–101]. The $\Delta N^2\text{LO}_{\text{GO}}$ Hamiltonian [35] is constructed at $N^2\text{LO}$ with explicit inclusion of Δ isobars in the EFT and is fit to few-body data and nuclear matter properties and optimized to reproduce bulk properties in medium-mass nuclei. Differences in results obtained by the two Hamiltonians reflect the underlying EFT uncertainty for nuclear forces.

We employ two valence spaces: VS1 with a ${}^{132}\text{Sn}$ core and an active valence space consisting of $1g_{7/2}$, $2d_{5/2}$, $2d_{3/2}$, $3s_{1/2}$, $1h_{11/2}$ proton orbitals and $2f_{7/2}$, $1h_{9/2}$, $1i_{13/2}$, $2f_{5/2}$, $3p_{3/2}$, $3p_{1/2}$ neutron orbitals; and VS2 with a ${}^{154}\text{Gd}$ core and an active valence space consisting of $2d_{3/2}$, $3s_{1/2}$, $1h_{11/2}$ proton orbitals and $1h_{9/2}$, $1i_{13/2}$, $2f_{5/2}$, $3p_{3/2}$, $3p_{1/2}$ neutron orbitals. Varying the valence space allows us to assess some of the uncertainty due to the employed many-body approximation. Recent developments have made IMSRG calculations at the normal-ordered three-body level available [36]. These calculations can currently not be converged in Yb, but we performed restricted calculations to estimate the order of magnitude of truncated contributions in the IMSRG, another source of many-body uncertainties.

To compute $\langle r^2 \rangle$ and $\langle r^4 \rangle$, we evaluate the ground-state expectation values of the translationally invariant point-proton radius operators r_p^2 and r_p^4 , with the definitions

$$r_p^2 = \sum_i \left[(1 + \tau_i) \frac{1}{2Z} \left(1 - \frac{2}{A} \right) + \frac{1}{A^2} \right] \mathbf{r}_i^2 + \sum_{i < j} \left[\frac{2}{A^2} - \frac{2}{AZ} \left(1 + \frac{\tau_i + \tau_j}{2} \right) \right] \mathbf{r}_i \cdot \mathbf{r}_j, \quad (\text{H1})$$

$$r_p^4 = \sum_i \left[(1 + \tau_i) \frac{1}{2Z} \left(1 - \frac{4}{A} \right) \right] \mathbf{r}_i^4 + \sum_{i < j} \frac{-2}{AZ} \left[(1 + \tau_i) \mathbf{r}_i^2 + (1 + \tau_j) \mathbf{r}_j^2 \right] \mathbf{r}_i \cdot \mathbf{r}_j + \mathcal{O}(A^{-3}). \quad (\text{H2})$$

We neglect the indicated higher-order contributions in r_p^4 , which would also include three- and four-body parts but are strongly suppressed. For $\langle r^2 \rangle$, we also include the spin-orbit [68] and relativistic Darwin-Foldy [69] corrections and account for the finite size of nucleons.

Our computed values of $\langle r^2 \rangle$, $\langle r^4 \rangle$, $\delta \langle r^2 \rangle$, and $\delta \langle r^4 \rangle$ are given in Tables H9 and H10. We note that we obtained nonphysical results for ${}^{168}\text{Yb}$ with the $\Delta N^2\text{LO}_{\text{GO}}$ Hamiltonian, with an inversion of proton $2d_{3/2}$ and $1h_{11/2}$ single-particle orbitals at the Hartree-Fock level relative to ${}^{170-176}\text{Yb}$. For the $\delta \langle r^2 \rangle$ and

$\delta \langle r^4 \rangle$ values in Tab. H10, we obtain extrapolated values for $\Delta N^2\text{LO}_{\text{GO}}$ based on the differences observed for (172,170) and (170,168) for the 1.8/2.0 (EM) Hamiltonian in the same valence space. Our results are compared with experimental measurements of $\delta \langle r^2 \rangle$ from Ref. [32] and our extraction of $\delta \langle r^4 \rangle$ trends in Fig. J6 and Fig. J5, respectively.

To assess theoretical uncertainties, we employ a correlated statistical uncertainty model. For the propagation of uncertainties in $\delta \langle r^2 \rangle$ and $\delta \langle r^4 \rangle$ to King-plot analyses, it is essential to account for correlations across isotope pairs. Errors due to truncations in *ab initio* nuclear theory are very systematic in nature, producing similar errors in neighboring isotopes. As a result, strong correlations arise, and we attempt to quantify and account for these in the following.

We assume that a prediction for given observable $\mathbf{o} = (o^{(170,168)}, o^{(172,170)}, o^{(174,172)}, o^{(176,174)})$ (true value unknown) can be understood as

$$\mathbf{o} = \tilde{\mathbf{o}} + \boldsymbol{\varepsilon}_{\text{EFT}} + \boldsymbol{\varepsilon}_{\text{VS}} + \boldsymbol{\varepsilon}_{\text{MB}}, \quad (\text{H3})$$

where $\tilde{\mathbf{o}}$ is the approximate prediction and $\boldsymbol{\varepsilon}_{\text{EFT}}$, $\boldsymbol{\varepsilon}_{\text{VS}}$, and $\boldsymbol{\varepsilon}_{\text{MB}}$ are errors made due the necessary truncations in the EFT for the Hamiltonians, the valence space, and the many-body method, respectively. We choose

$$\tilde{\mathbf{o}} = 0.75 \mathbf{o}_{1.8/2.0(\text{EM}),\text{VS1}} + 0.25 \mathbf{o}_{\Delta N^2\text{LO}_{\text{GO}},\text{VS1}} \quad (\text{H4})$$

based on the reproduction of experimental $\delta \langle r^2 \rangle$ values. Additionally, we model the EFT, valence-space, and many-body errors as random variables distributed as multivariate normal distributions,

$$\boldsymbol{\varepsilon}_{\text{EFT}} \sim \mathcal{N}(0, \Sigma_{\text{EFT}}), \quad (\text{H5})$$

$$\boldsymbol{\varepsilon}_{\text{VS}} \sim \mathcal{N}(0, \Sigma_{\text{VS}}), \quad (\text{H6})$$

$$\boldsymbol{\varepsilon}_{\text{MB}} \sim \mathcal{N}(0, \Sigma_{\text{MB}}). \quad (\text{H7})$$

We use full covariance matrices Σ to allow us to consider correlations across isotope pairs in our error model, which we discuss below.

We estimate the variances (i.e., $\boldsymbol{\sigma}_i^2 = \text{diag}(\Sigma_i)$) for our EFT and valence-space errors as

$$\boldsymbol{\sigma}_{\text{EFT}}^2 = (\mathbf{o}_{1.8/2.0(\text{EM}),\text{VS1}} - \mathbf{o}_{\Delta N^2\text{LO}_{\text{GO}},\text{VS1}})^2, \quad (\text{H8})$$

$$\boldsymbol{\sigma}_{\text{VS}}^2 = (\mathbf{o}_{1.8/2.0(\text{EM}),\text{VS1}} - \mathbf{o}_{1.8/2.0(\text{EM}),\text{VS2}})^2. \quad (\text{H9})$$

To estimate $\boldsymbol{\sigma}_{\text{MB}}^2$, we performed IMSRG(3)- N^7 calculations for ${}^{172}\text{Yb}$ [36]. IMSRG(3) calculations cannot currently be converged in Yb, but by including restricted three-body operators in the calculations, we gain insight into the magnitude of the IMSRG(3) corrections. Moreover, calculations in carbon and calcium have shown that the three-body corrections are strongly correlated across systems (with a correlation coefficient $r \geq 0.99$). We find the IMSRG(3) corrections for $\langle r^2 \rangle$ and $\langle r^4 \rangle$ in ${}^{172}\text{Yb}$ to be

Table H9: Absolute values of $\langle r^2 \rangle$ and $\langle r^4 \rangle$ for the 1.8/2.0 (EM) Hamiltonian using valence spaces VS1 and VS2 and for the $\Delta N^2 \text{LO}_{\text{GO}}$ Hamiltonian using VS1. Missing results for ^{168}Yb with the $\Delta N^2 \text{LO}_{\text{GO}}$ Hamiltonian are discussed in the main text.

Isotope A	$\langle r^2 \rangle$ [fm ²]		$\Delta N^2 \text{LO}_{\text{GO}}$ VS1
	1.8/2.0 (EM) VS1	VS2	
168	24.233	24.287	(*)
170	24.387	24.457	26.609
172	24.534	24.621	26.711
174	24.674	24.781	26.810
176	24.761	24.868	26.906
Isotope A	$\langle r^4 \rangle$ [fm ⁴]		$\Delta N^2 \text{LO}_{\text{GO}}$ VS1
	1.8/2.0 (EM) VS1	VS2	
168	710.4	719.5	(*)
170	719.3	728.9	850.9
172	727.8	738.4	857.4
174	736.2	747.8	863.6
176	743.3	755.5	869.6

on the order of 0.06 fm² and 2 fm⁴, respectively. Assuming a size extensive scaling of radius corrections and exploiting the strong correlation between neighboring isotopes, we find small many-body uncertainties σ_{MB}^2 for the differential quantities $\delta\langle r^2 \rangle$ and $\delta\langle r^4 \rangle$. All employed standard deviations are given in Tab. H11.

Finally, the covariance between $\varepsilon_i^{(A,A-2)}$ and $\varepsilon_i^{(B,B-2)}$ ($i \in \{\text{EFT}, \text{VS}\}$) is estimated as

$$\text{cov}(\varepsilon_i^{(A,A-2)}, \varepsilon_i^{(B,B-2)}) = r_i^{(A-B)/2} \sigma_i^{(A,A-2)} \sigma_i^{(B,B-2)}, \quad (\text{H10})$$

assuming an exponentially decaying correlation with a correlation r_i . Based on tests of different correlation values against our computed values, we found $r_{\text{EFT}} = 0.99$ and $r_{\text{VS}} = 0.97$. For the many-body uncertainties, we conservatively assumed no correlations.

We emphasize that these uncertainties and the underlying variances are not meant to be interpreted statistically but rather as an expert assessment of underlying parameters in our model to estimate correlated uncertainties and propagate those to King-plot nonlinearity analyses. We find this model to work well for $\delta\langle r^2 \rangle$ when compared to experimental values and expect it to work similarly well for $\delta\langle r^4 \rangle$.

Appendix I *Ab initio* atomic calculations of electronic coefficients

The dependence of isotope shifts on the nuclear structure parameters considered in this work is quantified by the electronic coefficients F , K , $G^{(2)}$, $G^{(4)}$, and D of Eq. (1). These can be calculated from atomic theory, however the accuracy is severely limited because of the

Table H10: $\delta\langle r^2 \rangle$ and $\delta\langle r^4 \rangle$ values for the 1.8/2.0 (EM) Hamiltonian using valence spaces VS1 and VS2 and for the $\Delta N^2 \text{LO}_{\text{GO}}$ Hamiltonian using VS1. Extrapolated results (*) for $(A, A') = (170, 168)$ for the $\Delta N^2 \text{LO}_{\text{GO}}$ Hamiltonian are discussed in the main text.

Isotope pair A, A'	$\delta\langle r^2 \rangle^{(A,A')} [fm^2]$		
	1.8/2.0 (EM) VS1	VS2	$\Delta N^2 \text{LO}_{\text{GO}}$ VS1
(170,168)	0.153	0.170	0.108(*)
(172,170)	0.148	0.164	0.103
(174,172)	0.140	0.160	0.099
(176,174)	0.087	0.087	0.096
Isotope pair A, A'	$\delta\langle r^4 \rangle^{(A,A')} [fm^4]$		
	1.8/2.0 (EM) VS1	VS2	$\Delta N^2 \text{LO}_{\text{GO}}$ VS1
(170,168)	8.85	9.48	6.81(*)
(172,170)	8.51	9.48	6.47
(174,172)	8.35	9.34	6.21
(176,174)	7.11	7.70	6.00

Table H11: Assessed standard deviations for $\delta\langle r^2 \rangle$ and $\delta\langle r^4 \rangle$ EFT, valence-space, and many-body errors.

Isotope pair A, A'	$\delta\langle r^2 \rangle^{(A,A')} [fm^2]$		
	$\sigma_{\text{EFT}}^{(A,A')}$	$\sigma_{\text{VS}}^{(A,A')}$	$\sigma_{\text{MB}}^{(A,A')}$
(170,168)	0.045	0.016	0.005
(172,170)	0.045	0.017	0.005
(174,172)	0.041	0.020	0.005
(176,174)	0.009	0.001	0.005
Isotope pair A, A'	$\delta\langle r^4 \rangle^{(A,A')} [fm^4]$		
	$\sigma_{\text{EFT}}^{(A,A')}$	$\sigma_{\text{VS}}^{(A,A')}$	$\sigma_{\text{MB}}^{(A,A')}$
(170,168)	2.04	0.63	0.15
(172,170)	2.04	0.97	0.16
(174,172)	2.14	0.98	0.16
(176,174)	1.11	0.58	0.16

strong many-body correlations. Worse, because parameters that depend on nuclear size and shape all depend on the wavefunction at the nucleus, the coefficients F and $G^{(4)}$ (and D at large m_ϕ) are nearly proportional to each other for different transitions. That means that quantities such as $G_{\gamma\alpha}^{(4)} = G_\gamma^{(4)} - F_{\gamma\alpha} G_\alpha^{(4)}$ that appear in the King linearity (see Eq. (2)) contain strong cancellations and therefore have large errors. A key advantage of the approach outlined in Appendix J is that the changes in $\delta\langle r^4 \rangle$ are extracted with the accuracy of $G_\alpha^{(4)}$ rather than $G_{\gamma\alpha}^{(4)}$.

We have used AMBiT [37] to perform a particle-hole configuration interaction (CI) calculation of these parameters for both Yb and Yb⁺. For both atom and ion, we start with a self-consistent Dirac-Fock calculation for the closed-shell core with 68 electrons (up to the filled $4f^{14}$ shell). We then generate $6s$, $6p$, and $5d$ valence orbitals by solving the Dirac-Fock equations in the potential of this core. An orbital basis is then constructed by multiplying these orbitals with simple

polynomials and orthogonality [102, 103]. The nuclear charge is represented by a Fermi-Dirac distribution.

For the case of transitions in Yb^+ (α, β, γ), we freeze the core $5sp4d$ orbitals¹. The $4f$ shell is treated as a (hole) valence shell. We allow single and double electron excitations up to $8spdf$ from leading configurations $6s, 5d, 6p, 4f^{-1} 6s^2, 4f^{-1} 6s 5d, 4f^{-1} 5d^2$, and $4f^{-1} 6p^2$, with the additional restriction that a maximum of two holes in the $4f$ shell were allowed. Configuration state functions, with defined angular momentum J and projection $M = J$ were formed from these configurations, and all were included in the CI Hamiltonian, which was then diagonalized to obtain level energies and wavefunctions. Coefficients calculated with this method are listed as “Fiducial” in Tab. I12.

For the fiducial calculations of Yb transitions (δ and ϵ) we can keep the $4f$ shell within the frozen core and treat the atom as having two valence electrons above closed shells. We use the same Dirac-Fock potential as in Yb^+ (in the case of Yb this is a V^{N-2} potential). We expand the virtual basis up to $12spdf$, and include all possible configurations of the two valence electrons within this basis.

To calculate electronic coefficients, we used both a finite field approach and an operator approach. In the finite field approach the nuclear radius is varied around the physical point and the coefficient is extracted by numerical derivative. For example, $F_\tau = d\omega_\tau/d\langle r^2 \rangle$ where ω_τ is the calculated transition frequency and r is the nuclear root-mean-square radius. This method is listed as “FF” in Tab. I12. The operator approach simply evaluates the expectation value of an effective operator at the physical point, for example, $F_\tau = \langle \delta V_{\text{nuc}} \rangle_i$, where δV_{nuc} is the change in the nuclear potential caused by $\delta\langle r^2 \rangle$. This method is listed as “(O)” in Tab. I12. We see a significant difference between the two, which is expected since the operator approach does not include core relaxation. Nevertheless, we include it here as a “worst case” indication of theoretical uncertainty.

To provide a more reliable uncertainty measure, we have performed very large CI calculations by including, in addition, all configurations that can be formed by taking single electron excitations from core orbitals and up to two excitations of valence electrons from the leading configurations. Here we are inspired by [104] who suggest using single core excitations to treat valence and core-valence correlations more efficiently. We also expect that by unfreezing the core, the calculations of short-range matrix elements could be improved. The results of our calculations that include these additional core-excited configurations are listed in Tab. I12 as “Core holes”. We see that generally, the difference between finite field and operator approaches to the matrix elements is smaller when using core holes, reflecting that the relaxation of

the core is partially included using this method. The exception is the γ transition for which we see a large difference: this transition directly involves a change in the occupancy of the $4f$ valence state, and the relaxation of this shell is large. Again we stress that our core hole approach is used as a measure of the theoretical uncertainty associated with having frozen cores in our fiducial CI method.

Appendix J Determining the evolution of $\delta\langle r^4 \rangle$ along the isotope chain from King plot data

Assuming that the leading source of nonlinearity in the King plot is $\delta\langle r^4 \rangle$, we can use isotope shift measurements to extract information on this quantity. We proceed in two steps: Using the precise nuclear mass and frequency measurements presented in this work, we construct the quantities

$$\hat{\nu}_\tau^{a,r} = \nu_\tau^a - \frac{w^a}{w^r} \nu_\tau^r, \quad (\text{J11})$$

where τ is the transition index, $r = (174, 176)$ denotes the reference isotope pair, and $a \in \{(168, 170), (170, 172), (172, 174)\}$ is an isotope pair index. Approximating Eq. (1) (with $\alpha \rightarrow \tau$) by

$$\nu_\tau^a \approx F_\tau \delta\langle r^2 \rangle^a + K_\tau w^a + G_\tau^{(4)} \delta\langle r^4 \rangle^a, \quad (\text{J12})$$

we obtain

$$\hat{\nu}_\tau^{a,r} \approx F_\tau D^{a,r} + G_\tau^{(4)} Q^{a,r}, \quad (\text{J13})$$

where the isotope-pair dependent quantity

$$D^{a,r} = \delta\langle r^2 \rangle^a - \frac{w^a}{w^r} \delta\langle r^2 \rangle^r, \quad (\text{J14})$$

can be constructed from the charge radius measurements tabulated in Ref. [32], and

$$Q^{a,r} = \delta\langle r^4 \rangle^a - \frac{w^a}{w^r} \delta\langle r^4 \rangle^r \quad (\text{J15})$$

describes the evolution of the nuclear deformation parameter $\delta\langle r^4 \rangle$ along the isotope chain. Following the King-plot approach, we perform a linear fit in isotope pair space, i.e., we fit F_τ to

$$\hat{\nu}_\tau^r \approx F_\tau \mathbf{D}^r, \quad (\text{J16})$$

where $\mathbf{x}^r = (x^{a,r}, x^{b,r}, x^{c,r}, x^{d,r})$, $x \in \{\hat{\nu}_\tau, D\}$. In this way, the precision of the isotope-shift measurements and nuclear mass measurements is exploited and field shift

¹In this notation the integers refer to the highest principal quantum numbers of the orbitals that follow. Here it refers to $1s - 5s$, $2p - 5p$, and $3d - 4d$.

τ	F_τ [GHz/fm ²]				$G_\tau^{(2)}$ [MHz/fm ⁴]				$G_\tau^{(4)}$ [MHz/fm ⁴]	
	Fiducial		Core holes		Fiducial		Core holes		Fiducial	Core holes
	FF	$\langle F \rangle$	FF	$\langle F \rangle$	FF	$\langle G^{(2)} \rangle$	FF	$\langle G^{(2)} \rangle$	$\langle G^{(4)} \rangle$	$\langle G^{(4)} \rangle$
α	-14.69	-13.09	-16.22	-16.14	81.8	72.4	90.3	89.2	8.76	10.80
β	-14.91	-13.07	-16.51	-16.45	83.0	72.3	91.8	90.9	8.75	11.00
γ	37.78	29.09	33.24	45.45	-209.7	-160.8	-184.5	-250.7	-19.47	-30.38
δ	-9.73	-10.62	-9.82	-11.3	54.2	58.8	54.9	62.2	7.12	7.57
ϵ	-13.54	-14.82	-13.69	-15.55	75.3	81.9	76.3	85.9	9.91	10.41

Table I12: Electronic field shift coefficients F_τ , quadratic field shift coefficients $G_\tau^{(2)}$, and $G_\tau^{(4)}$ -coefficients of the transitions τ defined in Tab. G8.

coefficients F_τ with relative uncertainties at the level of $\approx 0.3\%$ can be obtained.

Next, we subtract the fit results from the $\hat{\nu}^{a,r}$ and obtain the residuals

$$\hat{\nu}_\tau^{a,r} - F_\tau D^{a,r} = G_\tau^{(4)} Q^{a,r}. \quad (\text{J17})$$

Making use of the calculated electronic coefficients $G_\tau^{(4)}$, which are listed in Tab. I12 we deduce three independent objects $Q^{a,r}$ per isotope shift transition τ . Fixing $r = (174, 176)$ and $\tau = \alpha_{\text{PTB}}$ and choosing a value $\delta\langle r^4 \rangle^r = -7 \text{ fm}^4$, we are able to extract $\delta\langle r^4 \rangle$ values for the remaining isotope pairs, given in Tab. J13. We choose the reference value $\delta\langle r^4 \rangle^r = -7 \text{ fm}^4$ informed by predictions from *ab initio* nuclear structure theory and density functional theory shown in Fig. J5, which all predict this value to lie between $6 - 8 \text{ fm}^4$. Beyond this chosen reference value, uncertainties and covariances are obtained by propagating uncertainties from experimental input (ν_τ^a , w^a , and $\delta\langle r^2 \rangle^a$) and atomic theory ($G_\tau^{(4)}$) assuming independent normal distributions. The dominant source of uncertainty is $\delta\langle r^2 \rangle^{(170,168)}$, and we also understand this uncertainty to lead to correlations in the fit in Eq. (J16), leading to the considerable anti-correlation between $\delta\langle r^4 \rangle^{(170,168)}$ and $\delta\langle r^4 \rangle^{(172,170)}$.

We note that the approach outlined here to extract information on $\delta\langle r^4 \rangle$ from a King-plot nonlinearity is unable to give information on the absolute scale of $\delta\langle r^4 \rangle$. This is simply because we are considering only the nonlinearity, but $\delta\langle r^4 \rangle$ also produces an isotope shift contribution parallel to the linear field shift. We are unable to disentangle this contribution from the dominant field shift, so our approach is only able to make statements about how $\delta\langle r^4 \rangle$ changes across the isotopic chain.

These values are compared with predictions for *ab initio* nuclear structure theory and density functional theory in Fig. J5. Our extracted $\delta\langle r^4 \rangle$ values show a weak decrease between $\delta\langle r^4 \rangle^{(172,170)}$ and $\delta\langle r^4 \rangle^{(174,172)}$ and otherwise flat trend in $\delta\langle r^4 \rangle$ across the ytterbium isotopes studied here. Comparing this to the discussed nuclear structure calculations, we find that the flatter $\delta\langle r^4 \rangle$ trends of *ab initio* calculations more closely reproduce the extracted trends.

Table J13: Experimental $\delta\langle r^4 \rangle^{A,A-2}$ values relative to $\delta\langle r^4 \rangle^{176,174} = 7 \text{ fm}^4$ extracted from isotope shifts from the α_{PTB} transitions using atomic theory with uncertainties and covariances propagated from input uncertainties.

Isotope pair $a = (A, A')$	$\delta\langle r^4 \rangle^a$ [fm ⁴]	cov($\delta\langle r^4 \rangle^a$, $\delta\langle r^4 \rangle^b$) [fm ⁸]		
		Isotope pair $b = (A, A')$		
		(170,168)	(172,170)	(174,172)
(170,168)	7.33 (27)	0.076	-0.088	-0.010
(172,170)	7.53 (32)	-0.088	0.104	0.006
(174,172)	6.97 (28)	-0.010	0.006	0.079
(176,174)	7 (reference)			

Appendix K Bounds on the new boson

The spectroscopy bounds in Fig. 3 were derived by constructing generalized King plots [10], which require the isotope shift and mass measurements of n pairs of stable spinless isotopes on $n - 1$ transitions to eliminate $n - 2$ nuclear factors from the system of isotope shift equations. In ytterbium, it is currently the number of suitable isotope pairs, $n = 4$, that fixes the maximal dimension of the generalized King plot: using the frequency measurements on 3 transitions, the charge radius variance $\delta\langle r^2 \rangle$, as well as the leading King nonlinearity, induced by $\delta\langle r^4 \rangle$, can be eliminated. The remaining King nonlinearity is used to set upper bounds on the coupling α_{NP} of the new boson to electrons and neutrons. This method is particularly useful since it is fully data-driven: The subtraction of additional calculated SM effects such as $\delta\langle r^2 \rangle^2$ from the remaining King nonlinearity would reduce the precision of the experiment to the level of the theory uncertainties on said SM terms and hence not improve the bounds.

The red curve in Fig. 3 shows the bound on the new boson obtained by applying the generalized King plot method [10] to the frequency and mass measurements presented in this work, combined with frequency measurements presented in Ref. [30]. This bound is compared with previous generalized King plot bounds using Ca^+ data [38, 39] and Yb^+ data [8, 30]. Note that the same transitions were used for the orange and red curves. The locations of the characteristic peaks differ at the upper end of the plotted m_ϕ values due to an offset between

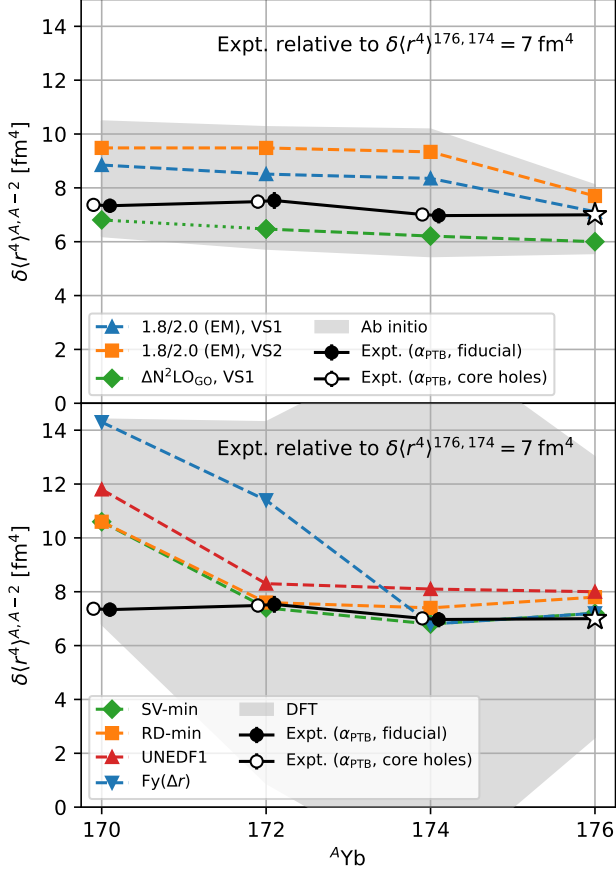


Fig. J5: Experimental $\delta\langle r^4 \rangle^{A,A-2}$ values relative to $\delta\langle r^4 \rangle^{176,174} = 7 \text{ fm}^4$ extracted from isotope shifts from the α transitions using atomic theory (fiducial, core holes) are compared to nuclear theory predictions from our *ab initio* calculations [top, 1.8/2.0 (EM), VS1 and VS2; $\Delta\text{N}^2\text{LO}_{\text{GO}}$, VS1] and from density functional theory calculations [8] [bottom, SV-min, RD-min, UNEDF1, $\text{Fy}(\Delta r)$] for $A \in \{170, 172, 174, 176\}$. The gray bands give estimated uncertainties of the theory results.

the α_{MIT} and α_{PTB} measurements. When this offset is taken into account, the slopes of the two curves agree.

The competing 2σ bounds are shown as exclusion regions. The combination of the bound on y_e from the measurement of the anomalous magnetic moment of the electron, $(g-2)_e$ [40, 41], and the bound on y_n [2] from neutron optics [42] and neutron scattering experiments [42–45] is indicated in yellow. For masses $m_\phi < 10^2 \text{ eV}/c^2$, fifth force searches via the Casimir effect provide particularly strong bounds (green) [46, 47]. Beam dump experiments provide competitive bounds for $2m_e \lesssim m_\phi$. These are not shown in Fig. 3 due to their dependence on the lifetime of the new boson ϕ , which is a function of all couplings of ϕ , not only of the couplings to electrons and neutrons.

Not shown either are the bounds from hydrogen-deuterium (HD) isotope shifts [105]. For light elements, there are not sufficiently many isotopes to construct a King plot, but the precision of the theory predictions

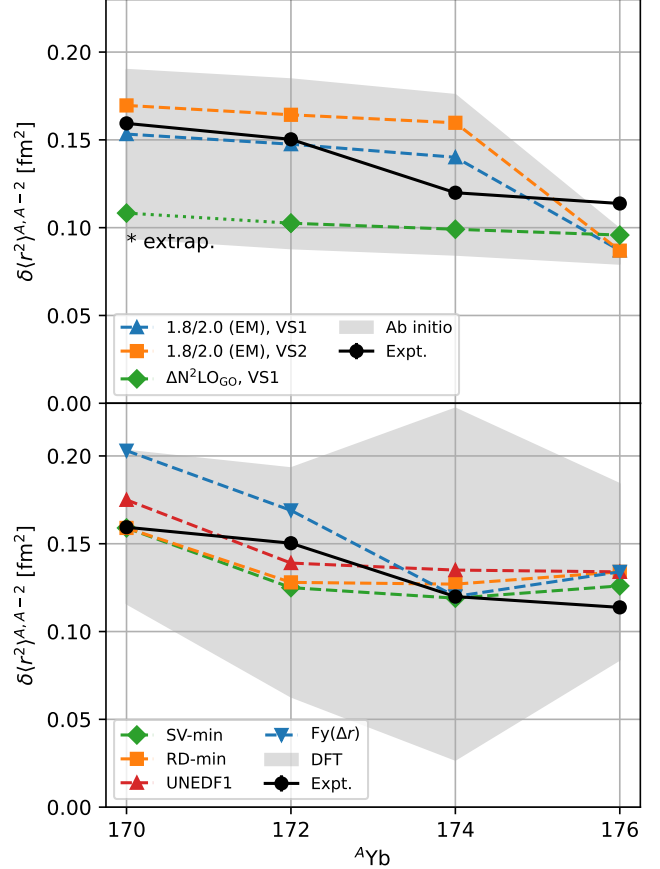


Fig. J6: Experimental $\delta\langle r^2 \rangle^{A,A-2}$ values [32] are compared to nuclear theory predictions from our *ab initio* calculations [top, 1.8/2.0 (EM), VS1 and VS2; $\Delta\text{N}^2\text{LO}_{\text{GO}}$, VS1] and from density functional theory calculations [8] [bottom, SV-min, RD-min, UNEDF1, $\text{Fy}(\Delta r)$] for $A \in \{170, 172, 174, 176\}$. The gray bands give estimated uncertainties of the theory results.

reaches the level of the experimental precision, such that the direct comparison of the two can be used to set a bound. This bound, however, depends on the measured HD charge radius difference which is determined via electron scattering or via muonic atom spectroscopy. As the former leads to a weaker bound than the bound from $(g-2)_e$ times neutron scattering, and the latter depends on the new boson's coupling to muons, the HD bounds are omitted in Fig. 3.

The blue-shaded areas in Fig. 3 are disfavored by astrophysical considerations, such as bounds from star cooling in horizontal branch stars (globular cluster) [48, 49] and from energy loss in the core of the supernova SN1987a [50], which is subject to an $\mathcal{O}(1)$ uncertainty [106]. Complementary bounds from laboratory experiments would provide valuable contributions to the search for new bosons also in these regions of parameter space.

Finally, the green dashed lines in Fig. 3 show the bounds on y_e from the anomalous magnetic moment of the electron [40, 41], $(g-2)_e$, multiplied by the bounds

on y_n from the kaon decay $K \rightarrow \pi + \text{invisible}$, which can be estimated using the bounds on the new boson couplings to quarks and the first coefficient of the QCD β -function [107]. These bounds are highly dependent on the flavor structure of the couplings of the new boson ϕ to the quarks. For illustration, Fig. 3 shows the bound on $\alpha_{\text{NP}}/\alpha_{\text{EM}}$ in the presence of a coupling to top-quarks, y_t , and the bound in presence of a coupling to up-quarks, y_u . They differ by approximately seven orders of magnitude.

This leaves open regions of parameter space where King plots have the potential of providing the most competitive bounds on ϕ , that are agnostic both of its decay widths into dark matter and of the flavor structure of its couplings to quarks. In the future, the King plot bounds can be further improved by increasing the dimension of the generalized King plots. This can be achieved by expanding the experimental program to isotopes with long half-lives (e.g. ^{166}Yb), or by moving to new atomic systems such as Sn [53] or Xe [54], both of which have seven, spinless stable isotopes and suitable clock transitions.